

Research Article

Pyronaridine Protects Against SARS-CoV-2 in Mouse

Ana C. Puhl^{1*#}, Giovanni F. Gomes^{2*}, Samara Damasceno², Andre S. Godoy³, Gabriela D. Noske³, Aline M. Nakamura³, Victor O. Gawriljuk³, Rafaela S. Fernandes³, Natalia Monakhova⁴, Olga Riabova⁴, Thomas R. Lane¹, Vadim Makarov⁴, Flavio P. Veras², Sabrina S. Batah⁵, Alexandre T. Fabro⁵, Glaucius Oliva³, Fernando Q. Cunha², José C. Alves-Filho^{2#} Thiago M. Cunha^{2#} and Sean Ekins^{1#}.

¹Collaborations Pharmaceuticals, Inc., 840 Main Campus Drive, Lab 3510, Raleigh, NC 27606, USA.

² Center for Research in Inflammatory Diseases (CRID), Ribeirao Preto Medical School, University of Sao Paulo, Avenida Bandeirantes, 3900, Ribeirao Preto, 14049-900 ; Sao Paulo, Brazil.

³ Institute of Physics of Sao Carlos, University of Sao Paulo, Av. Joao Dagnone, 1100 - Jardim Santa Angelina, Sao Carlos, 13563-120, Brazil.

⁴ Research Center of Biotechnology RAS, 119071 Moscow, Russia.

⁵ Department of Pathology and Legal Medicine, Ribeirão Preto Medical School, University of São Paulo, Ribeirão Preto, Brazil.

* Both authors contribute equally

#To whom correspondence should be addressed: Ana C. Puhl, E-mail address: ana@collaborationspharma.com; Thiago M. Cunha E-mail address: thicunha@fmrp.usp.br; Sean Ekins, E-mail address: sean@collaborationspharma.com,

Short running title: Pyronaridine *in-vivo* efficacy against SARS-CoV-2

KEYWORDS

Antiviral, SARS-CoV-2, Spike protein, pyronaridine

ABBREVIATIONS USED

Angiotensin converting enzyme 2 (ACE2); Bis(monoacylglycero)phosphate (BMP); Coronavirus disease (COVID-19); Middle East Respiratory Syndrome coronavirus (MERS-CoV); Severe Acute Respiratory coronavirus 2 (SARS-CoV-2).

Abstract

There are currently relatively few small-molecule antiviral drugs that are either approved or emergency approved for use against SARS-CoV-2. One of these is remdesivir, which was originally repurposed from its use against Ebola and functions by causing early RNA chain termination. We used this as justification to evaluate three molecules we had previously identified computationally with antiviral activity against Ebola and Marburg. Out of these we previously identified pyronaridine, which inhibited the SARS-CoV-2 replication in A549-ACE2 cells. Herein, the *in vivo* efficacy of pyronaridine has now been assessed in a K18-hACE transgenic mouse model of COVID-19. Pyronaridine treatment demonstrated a statistically significant reduction of viral load in the lungs of SARS CoV-2 infected mice. Furthermore, the pyronaridine treated group reduced lung pathology, which was also associated with significant reduction in the levels of pro-inflammatory cytokines/chemokine and cell infiltration. Notably, pyronaridine inhibited the viral PL^{pro} activity *in vitro* (IC₅₀ of 1.8 μM) without any effect on M^{pro}, indicating a possible molecular mechanism involved in its ability to inhibit SARS-CoV-2 replication. Interestingly, pyronaridine also selectively inhibits the host kinase CAMK1 (IC₅₀ of 2.4 μM). We have also generated several pyronaridine analogs to assist in understanding the structure activity relationship for PL^{pro} inhibition. Our results indicate that pyronaridine is a potential therapeutic candidate for COVID-19.

One sentence summary:

There is currently intense interest in discovering small molecules with direct antiviral activity against the severe acute respiratory syndrome coronavirus 2 (SARS-Cov-2). Pyronaridine, an antiviral drug with in vitro activity against Ebola, Marburg and SARS-CoV-2 has now statistically significantly reduced the viral load in mice along with IL-6, TNF- α , and IFN- β ultimately demonstrating a protective effect against lung damage by infection to provide a new potential treatment for testing clinically.

Introduction

At the time of writing, we are in the midst of a major a global health crisis caused by the virus Severe Acute Respiratory Syndrome Coronavirus 2 (SARS-CoV-2) that was originally reported in Wuhan, China in late 2019 (1, 2). Infection with this virus leads to extensive morbidity, mortality and a very broad range of clinical symptoms such as cough, loss of smell and taste, respiratory distress, pneumonia and extrapulmonary events characterized by a sepsis-like disease collectively called 2019 coronavirus disease (COVID-19) (3). In the USA, there are currently three vaccines available, one of which has recently obtained full approval from the FDA to protect against SARS-CoV-2 (4-6). There are however few small-molecule drugs approved for COVID-19 (7) including remdesivir (8), which originally demonstrated activity in Vero cells (9, 10), human epithelial cells and in Calu-3 cells (10) infected with SARS-CoV-2 prior to clinical testing. Remdesivir represents a repurposed drug which was originally developed for Hepatitis C virus but was then repurposed for treating Ebola and has since reached clinical trials (11). We therefore hypothesized that other drugs that were effective against Ebola might also be prioritized for evaluation *in vitro* against SARS-CoV-2. Previously, we had used a machine-learning model to identify tilorone, quinacrine and pyronaridine tetraphosphate(12) for testing against Ebola virus (EBOV) and subsequently these three inhibited EBOV and Marburg *in vitro* as well as demonstrating significant efficacy in the mouse-adapted EBOV (ma-EBOV) model (13-15). All of these molecules were identified as lysosomotropic, a characteristic that suggests these could be possible entry inhibitors (16). Pyronaridine tetraphosphate is used as an antimalarial in several countries as part of a combination therapy with artesunate (Pyramax). Pyronaridine alone also

demonstrated significant activity in the guinea pig-adapted model of EBOV infection (17). We and others (18-20) have recently shown that these compounds possess *in vitro* activity against SARS-CoV-2 and tilorone and pyronaridine are in clinical trials, the latter in combination with artesunate. The C_{max} data for pyronaridine in our previous mouse pharmacokinetics studies (i.p. dosing) suggests that plasma levels that are above the average IC_{50} observed for SARS-CoV-2 inhibition *in vitro* (13) can be reached with dosing well below the maximum tolerated dose. Pyronaridine also has excellent *in vitro* ADME properties with a long half-life that makes a single dose treatment possible (13, 18). We now expand on our earlier *in vitro* characterization of pyronaridine (18) by assessing the *in vivo* efficacy in a mouse model of COVID-19. Finally, in an attempt to further explore molecular mechanisms, we tested the activity of pyronaridine *in vitro* against viral and host targets.

***In vivo* efficacy of Pyronaridine in a mouse model of COVID-19**

In vivo efficacy was assessed in K-18-hACE2 mouse model of COVID-19 (21-23). Pyronaridine (75 mg/kg, i.p) (13) was administered 1 h prior to infection. Mice that were given pyronaridine, received a single treatment. On the third day post-infection, mice were euthanized and lung viral load, cytokine levels and histopathology were evaluated (Figure 1A). In all groups tested, mice lost weight compared to uninfected animals that received only vehicle formulation (Figure 1B). Lung viral load was evaluated by RT-qPCR and the pyronaridine treated group showed a statistically significant decrease in the lung viral load (Figure 1C). Moreover, reduced levels of INF-1 β were observed in infected mice, and pyronaridine restored the levels of INF-1 β close to that found in uninfected animals (Figure 1D). Interestingly, the increased levels of IL-6 found in the infected untreated

group were not observed in animals treated with pyronaridine (Figure 1E). In addition, pyronaridine reduced the high levels of CXCL1 and CCL4 observed in infected animals (Figure 1D). Pyronaridine did not however reduce the high levels of IL-10, TNF- α , CCL2, and CCL3 (Figure 1F, G, K, L, M) below the elevated levels found in the infected mice.

To determine the severity of lung damage, histological examination of hematoxylin and eosin (H&E) stained lung tissue was performed. Infected, untreated mice showed severe pathological changes with inflammatory cell infiltrates. In contrast, pyronaridine-treated animals exhibited improved morphology and milder infiltration (Figure 2A). Histological observations were confirmed by quantitative morphometric analysis of the H&E-stained slides showing a statistically significant reduction in inflammation (Figure 2B).

Pyronaridine potentially targets SARS-CoV-2 PL^{pro} but not M^{pro}

SARS-CoV-2 proteases M^{pro} and PL^{pro} are essential for viral replication and have been widely studied for the discovery of new direct acting antivirals (24-26). Pyronaridine was therefore tested against both SARS-CoV-2 recombinant PL^{pro} and M^{pro} through FRET-based *in vitro* assays. Pyronaridine inhibited PL^{pro} with an IC₅₀ of 1.86 ± 0.58 μ M (Figure 3A) but did not show any appreciable activity against M^{pro} at 20 μ M (data not shown). Additional analogs of pyronaridine were also synthesized and tested against PL^{pro}. The analogs 12126038, 12126039 and 12126040 showed similar inhibitory activity when compared with pyronaridine (as well as that reported for GRL0617 (27)), indicating that the aminophenol moiety together with pyrrole or tertiary amine substitutions at the meta position are tolerated for PL^{pro} inhibition (Table 1, Figure 3A). The deletion of these groups

in analogs 10326099, 12126035, 12126036, 12126037 and 12126072 caused complete abolishment of the inhibitory activity of the series (Table 1). The PL^{pro} active site contains four subsites for peptide recognition, with a strong preference for positively charged amino acids at P3 and P4 subsites (24-26). In our molecular docking studies (Figure 3B), the positions where the 2,6-bis[(pyrrolidin-1-yl)methyl]phenol moiety of pyronaridine were docked at the P4 subsite showed a far higher score than the second highest cluster group (Glide score of -5.052 and HADDOCK score of -65.6). These positively charged amino-groups would likely satisfy the negatively charged cavity that forms the P4 subsite, forming hydrogen bounds with Asp164 and π -stacking with Tyr26 (Figure 3C). Compounds 12126038 and 12126039 also showed very similar poses after docking, indicating binding to the P4 subsite (Figure 3B). The primary docking poses from Glide for all compounds are provided in Fig. S1. These results indicate that the *in vitro* and *in vivo* efficacy of pyronaridine may be related to PL^{pro} inhibition.

Kinase activity profiling

Due to the possible effect of pyronaridine on cytokines (Figure 1) we have also assessed the effect on host targets, as SARS-CoV-2 can cause an imbalance in the immune system that may result in a cytokine storm(28) as well as leading to acute respiratory distress syndrome (ARDS), coagulation disorders, and eventually multiple organ failure (28, 29). Hence targeting the cytokine storm to address hyperinflammation represents another approach to the treatment of COVID-19 patients (30-33). In this regard, we have explored the effect of pyronaridine on human kinases which are responsible for host cell signaling (34, 35). Screening of pyronaridine (tested at 1 μ M) against 485 kinases identified only

2 as having mean percent inhibition greater than 30% including CAMK1 (35%) and MELK (31%) (Table S1). Subsequently, the IC₅₀ was determined for CAMK1 (2.4 µM) (Figure 4).

Discussion

Even with vaccines becoming widely available in many countries COVID-19 continues to exact a very heavy toll on those that are unvaccinated. We are in a race against time before the virus mutates and vaccines lose their effectiveness. There is therefore an urgent need for new antivirals and in particular small-molecule treatments that are orally delivered and can be used outside of a hospital setting. Finding, developing, and progressing small molecules to the clinic is generally a slow and expensive process (36), hence drug repurposing has been attempted by many groups to speed this up (either experimentally or computationally (37)) by identifying already approved or clinical stage candidates used for other applications or quickly follow up the few molecules that are being used already. The traditional prioritization of compounds *in vitro* before animal models and then humans is still repeated and so far with few successes with many molecules not demonstrating efficacy *in vivo* (38, 39).

Our understanding of the antiviral mechanism of pyronaridine previously shown to inhibit the Ebola virus *in vitro* and *in vivo* (13) via binding to the viral glycoprotein(16) as well as through its potent lysosomotropic activity (40) and now the *in vitro* activity against SARS-CoV-2 (18) is also further expanded. Pyronaridine was previously identified with *in vitro* activity against SARS-CoV-2 in A549-ACE2 cells that was on a par with remdesivir in this cell line (18). In the current study, we have demonstrated that pyronaridine also

has antiviral activity against SARS-CoV-2 *in vivo*. A single prophylactic dose of pyronaridine (75 mg/kg i.p) reduced the viral load in the lung of infected mice 3 days post-infection. *In vitro* assays suggest that pyronaridine possesses a direct antiviral effect showing activity against PL^{pro} (IC₅₀ 1.86 μ M, Figure 3), but did not inhibit SARS-CoV-2 M^{pro}. Kinase profiling, resulted in determination of IC₅₀ for CAMK1 (IC₅₀ 2.4 μ M, Figure 4).

A single dose (75 mg/kg i.p.) of pyronaridine has an elimination half-life of 146 h in mice (13), comparable to the reported half-life of pyronaridine in humans of 195-251 h (41, 42). A study of pyronaridine as a single oral dose (400 mg) given to a healthy volunteer found a C_{max} in plasma of 495.8 ng/ml at a T_{max} of 0.5 h (41, 43), which gives a concentration close to 1 μ M. In our study, pyronaridine inhibits PL^{pro} at 1.86 μ M and CAMK1 at 2.4 μ M, which is very close to the C_{max} of 1 μ M. Pyronaridine preferentially associates with blood cells and is highly plasma protein bound (43), which suggests that it may not reach the unbound concentration necessary to have an effect on PL^{pro} and CAMK1 at these doses. Activation of CAMK1 has been reported to negatively impact HBV biosynthesis (44, 45), however the mechanism has not been elucidated yet and the possible role of CAMK1 on SARS-CoV-2 infection remains to be investigated.

Several studies have shown a cytokine and chemokine storm as important during SARS-CoV-2 infection in patients with COVID-19, including PDGF, VEGF (46), IL-6 (47, 48), IL-8, IL-10 (48), TNF- α (48) and IFN- α and - β (49-53). Furthermore, an impaired type I interferon response has already been observed in COVID-19 (54), which is followed by increased circulating levels of IL-6 and TNF- α . Many viruses, including SARS-CoV-2, subvert the immune system by inhibiting the production of interferons (INF), an important

family of antiviral mediators (55-58), which results in an impaired antiviral defense and increased viral replication and infection. Here, we have demonstrated that pyronaridine restored the levels of INF-1 β in infected mice. Moreover, as already discussed, this effect was associated with a reduced viral load after the treatment with pyronaridine. Notably, pyronaridine also reverted the altered levels of IL-6 and CXCL1 observed in infected mice. In addition to biochemical changes, histopathological findings are also observed in the lung of patients (59-61) and in other experimental models of COVID-19 (21-23). In the present study, control animals infected with SARS-CoV-2 presented pronounced inflammatory cell infiltration and the histological examination of mouse lungs for those treated with pyronaridine showed milder infiltration, appearing comparable to that of uninfected mice. Thus, pyronaridine appears to have both antiviral and immunomodulatory effects in this experimental model of COVID-19 as used in the present study.

In summary, our present study provided additional data on the efficacy of pyronaridine against SARS-CoV-2 infection as well as highlighting reduced lung pathology and inflammation in a mouse model of COVID-19. Furthermore, we have shown that pyronaridine may target PI^{pro} as well as CAMK1. There are few inhibitors of CAMK1 that have been identified to date (such as Baretin (62) or pyridine amides (63)) which has a role in inflammation targeting IL-10 (62). Previous *in vitro* work has shown that inhibiting CAMK1 in cells reduces IL-10, the master anti-inflammatory interleukin (64). In the present study there is not a significant difference in the IL-10 levels between the untreated and pyronaridine-treated infected groups so it seems unlikely that CAMK1 inhibition would be involved in the mechanism of action of inhibition of SAR-CoV-2. In

conclusion, we propose that pyronaridine could be used alone as a potential therapeutic candidate for COVID-19. Finally, with the emerging virulence of novel SARS-CoV-2 strains, identifying repurposed drugs with novel mechanisms of action and whose antiviral activity translates from *in vitro* to *in vivo* are rare (39), and may lead to new treatments as well as their further optimization.

Competing interests:

SE is CEO of Collaborations Pharmaceuticals, Inc. ACP and TRL are employees at Collaborations Pharmaceuticals, Inc.

ACKNOWLEDGMENTS

The authors would like to kindly acknowledge their many collaborators around the world who have assisted in our various COVID-19 projects. The authors gratefully acknowledge the technical assistance of Marcella Daruge Grando, Ieda Regina dos Santos, Juliana Trench Abumansur, and Felipe Souza.

Grant information

We kindly acknowledge NIH funding: SE kindly acknowledges NIH funding R44GM122196-02A1 from NIH NIGMS 1R43AT010585-01 from NIH/NCCAM, AI142759 and AI108197 to RSB. Dr. Glaucius Oliva and colleagues acknowledge Coordenação de Aperfeiçoamento de Pessoal de Nível Superior (CAPES – project 88887.516153/2020-

00) and Fundação de Amparo à Pesquisa do Estado de São Paulo (FAPESP project 2013/07600-3). TMC, JCAF and FQC received funding from the São Paulo Research Foundation (FAPESP) under grant agreement 2013/08216-2 (Center for Research in Inflammatory Disease) and 2020/04860-8 and from Coordenação de Aperfeiçoamento de Pessoal de Nível Superior (project 88887.507155/2020-00). NM, OR and VM acknowledge RFBR (project 20-54-80006).

Author contributions:

A.C.P, T.M.C, S.E. conceived and codirected the study. A.C.P., G.F.G, A.S.G., V.M., G.O., F.Q.C., J.C.A.F, T.C designed the experiments; A.C.P, S.D., G.D.N., A.M.N, V.O.G, R.S.F, N.M., O.R, S.S.B and A.T.F performed *in vitro* experiments. G.F.G, S.D. F.P.V, performed *in vivo* experiments. A.C.P, S.E., G.F.G, A.S.G. and T.M.C, and T.L. wrote the manuscript. All authors read and accept the manuscript.

Competing interests:

SE is CEO of Collaborations Pharmaceuticals, Inc. ACP is an employee at Collaborations Pharmaceuticals, Inc. Collaborations Pharmaceuticals, Inc. has obtained FDA orphan drug designations for pyronaridine, tilorone and quinacrine for use against Ebola. CPI have also filed a provisional patent for use of these molecules against Marburg and other viruses. Other authors have no conflicts.

References

1. F. Wu *et al.*, Author Correction: A new coronavirus associated with human respiratory disease in China. *Nature* **580**, E7 (2020).
2. V. Coronaviridae Study Group of the International Committee on Taxonomy of, The species Severe acute respiratory syndrome-related coronavirus: classifying 2019-nCoV and naming it SARS-CoV-2. *Nat Microbiol* **5**, 536-544 (2020).
3. WHO, Naming the coronavirus disease (COVID-2019) and the virus that causes it. 2020 [https://www.who.int/emergencies/diseases/novel-coronavirus-2019/technical-guidance/naming-the-coronavirus-disease-\(covid-2019\)-and-the-virus-that-causes-it](https://www.who.int/emergencies/diseases/novel-coronavirus-2019/technical-guidance/naming-the-coronavirus-disease-(covid-2019)-and-the-virus-that-causes-it)
4. M. F. U. Rehman *et al.*, Novel coronavirus disease (COVID-19) pandemic: A recent mini review. *Comput Struct Biotechnol J* **19**, 612-623 (2021).
5. N. C. Kyriakidis, A. López-Cortés, E. V. González, A. B. Grimaldos, E. O. Prado, SARS-CoV-2 vaccines strategies: a comprehensive review of phase 3 candidates. *NPJ Vaccines* **6**, 28 (2021).
6. H. Y. Huang *et al.*, Landscape and progress of global COVID-19 vaccine development. *Hum Vaccin Immunother*, 1-5 (2021).
7. M. D. Hall *et al.*, Report of the National Institutes of Health SARS-CoV-2 Antiviral Therapeutics Summit. *J Infect Dis* **224**, S1-S21 (2021).
8. R. T. Eastman *et al.*, Remdesivir: A Review of Its Discovery and Development Leading to Emergency Use Authorization for Treatment of COVID-19. *ACS Cent Sci* **6**, 672-683 (2020).
9. M. Wang *et al.*, Remdesivir and chloroquine effectively inhibit the recently emerged novel coronavirus (2019-nCoV) in vitro. *Cell Res* **30**, 269-271 (2020).
10. A. J. Pruijssers *et al.*, Remdesivir Inhibits SARS-CoV-2 in Human Lung Cells and Chimeric SARS-CoV Expressing the SARS-CoV-2 RNA Polymerase in Mice. *Cell Rep* **32**, 107940 (2020).
11. S. Mulangu *et al.*, A Randomized, Controlled Trial of Ebola Virus Disease Therapeutics. *N Engl J Med* **381**, 2293-2303 (2019).
12. S. Ekins *et al.*, Machine learning models identify molecules active against Ebola virus in vitro. *F1000Res* **4**, 1091 (2015).
13. T. R. Lane *et al.*, Repurposing the antimalarial pyronaridine tetraphosphate to protect against Ebola virus infection. *PLoS Negl Trop Dis* **13**, e0007890 (2019).

14. T. R. Lane, J. E. Comer, A. N. Freiberg, P. B. Madrid, S. Ekins, Repurposing Quinacrine Against Ebola Virus Infection In vivo. *Antimicrob Agents Chemother* **63**, e01142-01119 (2019).
15. S. Ekins *et al.*, Efficacy of Tilorone Dihydrochloride against Ebola Virus Infection. *Antimicrob Agents Chemother* **62**, (2018).
16. T. R. Lane, S. Ekins, Towards the Target: Tilorone, Quinacrine and Pyronaridine Bind to Ebola Virus Glycoprotein. *ACS Med Chem Lett* **11**, 1653-1658 (2020).
17. T. R. Lane *et al.*, Efficacy of Oral Pyronaridine Tetrphosphate and Favipiravir Against Ebola Virus Infection in Guinea Pig *Antiviral Research* **181**, 104863 (2020).
18. A. C. Puhl *et al.*, Repurposing the Ebola and Marburg Virus Inhibitors Tilorone, Quinacrine, and Pyronaridine: In Vitro Activity against SARS-CoV-2 and Potential Mechanisms. *ACS Omega* **6**, 7454-7468 (2021).
19. S. Jeon *et al.*, Identification of antiviral drug candidates against SARS-CoV-2 from FDA-approved drugs. *Antimicrob Agents Chemother* **64**, e00819-00820 (2020).
20. J.-Y. Bae *et al.*, Pyronaridine and artesunate are potential antiviral drugs against COVID-19 and influenza. *bioRxiv*, 2020.2007.2028.225102 (2020).
21. P. B. McCray *et al.*, Lethal infection of K18-hACE2 mice infected with severe acute respiratory syndrome coronavirus. *J Virol* **81**, 813-821 (2007).
22. F. S. Oladunni *et al.*, Lethality of SARS-CoV-2 infection in K18 human angiotensin-converting enzyme 2 transgenic mice. *Nat Commun* **11**, 6122 (2020).
23. L. Bao *et al.*, The pathogenicity of SARS-CoV-2 in hACE2 transgenic mice. *Nature* **583**, 830-833 (2020).
24. Z. Jin *et al.*, Structure of M. *Nature* **582**, 289-293 (2020).
25. D. Shin *et al.*, Papain-like protease regulates SARS-CoV-2 viral spread and innate immunity. *Nature* **587**, 657-662 (2020).
26. J. Qiao *et al.*, SARS-CoV-2 M. *Science* **371**, 1374-1378 (2021).
27. Z. Fu *et al.*, The complex structure of GRL0617 and SARS-CoV-2 PLpro reveals a hot spot for antiviral drug discovery. *Nat Commun* **12**, 488 (2021).
28. V. J. Costela-Ruiz, R. Illescas-Montes, J. M. Puerta-Puerta, C. Ruiz, L. Melguizo-Rodríguez, SARS-CoV-2 infection: The role of cytokines in COVID-19 disease. *Cytokine Growth Factor Rev* **54**, 62-75 (2020).

29. R. Chen *et al.*, Cytokine Storm: The Primary Determinant for the Pathophysiological Evolution of COVID-19 Deterioration. *Front Immunol* **12**, 589095 (2021).
30. S. Felsenstein, J. A. Herbert, P. S. McNamara, C. M. Hedrich, COVID-19: Immunology and treatment options. *Clin Immunol* **215**, 108448 (2020).
31. A. E. Peter, B. V. Sandeep, B. G. Rao, V. L. Kalpana, Calming the Storm: Natural Immunosuppressants as Adjuvants to Target the Cytokine Storm in COVID-19. *Front Pharmacol* **11**, 583777 (2020).
32. N. Roshanravan, F. Seif, A. Ostadrahimi, M. Pouraghaei, S. Ghaffari, Targeting Cytokine Storm to Manage Patients with COVID-19: A Mini-Review. *Arch Med Res* **51**, 608-612 (2020).
33. N. Moradian *et al.*, Cytokine release syndrome: inhibition of pro-inflammatory cytokines as a solution for reducing COVID-19 mortality. *Eur Cytokine Netw* **31**, 81-93 (2020).
34. C. Beerli *et al.*, Vaccinia virus hijacks EGFR signalling to enhance virus spread through rapid and directed infected cell motility. *Nat Microbiol* **4**, 216-225 (2019).
35. S. Pleschka *et al.*, Influenza virus propagation is impaired by inhibition of the Raf/MEK/ERK signalling cascade. *Nat Cell Biol* **3**, 301-305 (2001).
36. S. M. Paul *et al.*, How to improve R&D productivity: the pharmaceutical industry's grand challenge. *Nat Rev Drug Discov* **9**, 203-214 (2010).
37. E. N. Muratov *et al.*, A critical overview of computational approaches employed for COVID-19 drug discovery. *Chem Soc Rev* **50**, 9121-9151 (2021).
38. T. A. Tummino *et al.*, Drug-induced phospholipidosis confounds drug repurposing for SARS-CoV-2. *Science* **373**, 541-547 (2021).
39. T. R. Lane, S. Ekins, Defending Antiviral Cationic Amphiphilic Drugs That May Cause Drug-Induced Phospholipidosis. *J Chem Inf Model*, (2021).
40. T. R. Lane *et al.*, Repurposing Pyramax® for the Treatment of Ebola Virus Disease: Additivity of the Lysosomotropic Pyronaridine and Non-Lysosomotropic Artesunate *Antiviral Research* **182**, 104908 (2020).
41. S. D. Jayaraman, S. Ismail, N. K. Nair, V. Navaratnam, Determination of pyronaridine in blood plasma by high-performance liquid chromatography for application in clinical pharmacological studies. *J Chromatogr B Biomed Sci Appl* **690**, 253-257 (1997).

42. S. Ramanathan *et al.*, A new and simple solid-phase extraction method for LC determination of pyronaridine in human plasma. *J Chromatogr B Analyt Technol Biomed Life Sci* **824**, 45-50 (2005).
43. S. L. Croft *et al.*, Review of pyronaridine anti-malarial properties and product characteristics. *Malar J* **11**, 270 (2012).
44. M. J. Bouchard, R. J. Puro, L. Wang, R. J. Schneider, Activation and inhibition of cellular calcium and tyrosine kinase signaling pathways identify targets of the HBx protein involved in hepatitis B virus replication. *J Virol* **77**, 7713-7719 (2003).
45. M. J. Bouchard, L. H. Wang, R. J. Schneider, Calcium signaling by HBx protein in hepatitis B virus DNA replication. *Science* **294**, 2376-2378 (2001).
46. C. Huang *et al.*, Clinical features of patients infected with 2019 novel coronavirus in Wuhan, China. *Lancet* **395**, 497-506 (2020).
47. T. Herold *et al.*, Elevated levels of IL-6 and CRP predict the need for mechanical ventilation in COVID-19. *J Allergy Clin Immunol* **146**, 128-136.e124 (2020).
48. J. Wang *et al.*, Specific cytokines in the inflammatory cytokine storm of patients with COVID-19-associated acute respiratory distress syndrome and extrapulmonary multiple-organ dysfunction. *Viral J* **18**, 117 (2021).
49. Q. Zhang *et al.*, Inborn errors of type I IFN immunity in patients with life-threatening COVID-19. *Science* **370**, (2020).
50. H. Xia *et al.*, Evasion of Type I Interferon by SARS-CoV-2. *Cell Rep* **33**, 108234 (2020).
51. C. K. Yuen *et al.*, SARS-CoV-2 nsp13, nsp14, nsp15 and orf6 function as potent interferon antagonists. *Emerg Microbes Infect* **9**, 1418-1428 (2020).
52. R. D. Molony *et al.*, Aging impairs both primary and secondary RIG-I signaling for interferon induction in human monocytes. *Sci Signal* **10**, (2017).
53. R. Hu, C. Q. Xia, E. Butfiloski, M. Clare-Salzler, Effect of high glucose on cytokine production by human peripheral blood immune cells and type I interferon signaling in monocytes: Implications for the role of hyperglycemia in the diabetes inflammatory process and host defense against infection. *Clin Immunol* **195**, 139-148 (2018).
54. J. Hadjadj *et al.*, Impaired type I interferon activity and inflammatory responses in severe COVID-19 patients. *Science* **369**, 718-724 (2020).
55. J. R. Teijaro, Type I interferons in viral control and immune regulation. *Curr Opin Virol* **16**, 31-40 (2016).

56. F. McNab, K. Mayer-Barber, A. Sher, A. Wack, A. O'Garra, Type I interferons in infectious disease. *Nat Rev Immunol* **15**, 87-103 (2015).
57. M. G. Katze, Y. He, M. Gale, Jr., Viruses and interferon: a fight for supremacy. *Nat Rev Immunol* **2**, 675-687 (2002).
58. J. S. Lee, E. C. Shin, The type I interferon response in COVID-19: implications for treatment. *Nat Rev Immunol* **20**, 585-586 (2020).
59. S. Caramaschi *et al.*, Histopathological findings and clinicopathologic correlation in COVID-19: a systematic review. *Mod Pathol* **34**, 1614-1633 (2021).
60. G. Pannone *et al.*, Lung histopathological findings in COVID-19 disease - a systematic review. *Infect Agent Cancer* **16**, 34 (2021).
61. L. P. Hariri *et al.*, Lung Histopathology in Coronavirus Disease 2019 as Compared With Severe Acute Respiratory Syndrome and H1N1 Influenza: A Systematic Review. *Chest* **159**, 73-84 (2021).
62. K. F. Lind, B. Osterud, E. Hansen, T. O. Jorgensen, J. H. Andersen, The immunomodulatory effects of barettin and involvement of the kinases CAMK1alpha and RIPK2. *Immunopharmacol Immunotoxicol* **37**, 458-464 (2015).
63. C. Fromont *et al.*, Discovery of Highly Selective Inhibitors of Calmodulin-Dependent Kinases That Restore Insulin Sensitivity in the Diet-Induced Obesity in Vivo Mouse Model. *J Med Chem* **63**, 6784-6801 (2020).
64. X. Zhang *et al.*, Calcium/calmodulin-dependent protein kinase (CaMK) Ialpha mediates the macrophage inflammatory response to sepsis. *J Leukoc Biol* **90**, 249-261 (2011).
65. F. S. Oladunni *et al.*, Lethality of SARS-CoV-2 infection in K18 human angiotensin-converting enzyme 2 transgenic mice. *Nat Commun* **11**, 6122 (2020).
66. L. Bao *et al.*, The pathogenicity of SARS-CoV-2 in hACE2 transgenic mice. *Nature* **583**, 830-833 (2020).
67. C. K. Yinda *et al.*, K18-hACE2 mice develop respiratory disease resembling severe COVID-19. *PLoS Pathog* **17**, e1009195 (2021).
68. V. M. Arce, J. A. Costoya, SARS-CoV-2 infection in K18-ACE2 transgenic mice replicates human pulmonary disease in COVID-19. *Cell Mol Immunol* **18**, 513-514 (2021).
69. G. B. Moreau *et al.*, Evaluation of K18-. *Am J Trop Med Hyg* **103**, 1215-1219 (2020).

70. E. S. Winkler *et al.*, Publisher Correction: SARS-CoV-2 infection of human ACE2-transgenic mice causes severe lung inflammation and impaired function. *Nat Immunol* **21**, 1470 (2020).
71. J. Zheng *et al.*, COVID-19 treatments and pathogenesis including anosmia in K18-hACE2 mice. *Nature* **589**, 603-607 (2021).
72. C. C. Hsia, D. M. Hyde, M. Ochs, E. R. Weibel, A. E. J. T. F. o. Q. A. o. L. Structure, An official research policy statement of the American Thoracic Society/European Respiratory Society: standards for quantitative assessment of lung structure. *Am J Respir Crit Care Med* **181**, 394-418 (2010).
73. R. A. Friesner *et al.*, Extra Precision Glide: Docking and Scoring Incorporating a Model of Hydrophobic Enclosure for Protein–Ligand Complexes. *Journal of Medicinal Chemistry* **49**, 6177-6196 (2006).
74. C. Dominguez, R. Boelens, A. M. J. J. Bonvin, HADDOCK: A Protein–Protein Docking Approach Based on Biochemical or Biophysical Information. *Journal of the American Chemical Society* **125**, 1731-1737 (2003).
75. G. D. Noske *et al.*, A Crystallographic Snapshot of SARS-CoV-2 Main Protease Maturation Process. *J Mol Biol* **433**, 167118 (2021).
76. ThermoFisher, Z'-LYTE Screening Protocol and Assay Conditions. 2018 http://assets.thermofisher.com/TFS-Assets/BID/Methods-&-Protocols/20180123_SSBK_Customer_Protocol_and_Assay_Conditions.pdf
77. ThermoFisher, Adapta Screening Protocol and Assay Conditions. 2018 http://assets.thermofisher.com/TFS-Assets/BID/Methods-&-Protocols/20180123_SSBK_Adapta_Customer_Protocol_and_Assay_Conditions.pdf
78. ThermoFisher, LanthaScreen Eu Kinase Binding Assay Screening Protocol and Assay Conditions. 2018 http://assets.thermofisher.com/TFS-Assets/BID/Methods-&-Protocols/20180123_SSBK_LanthaScreen_Binding_Customer_Protocol_and_Assay_Conditions.pdf

FIGURES AND LEGENDS

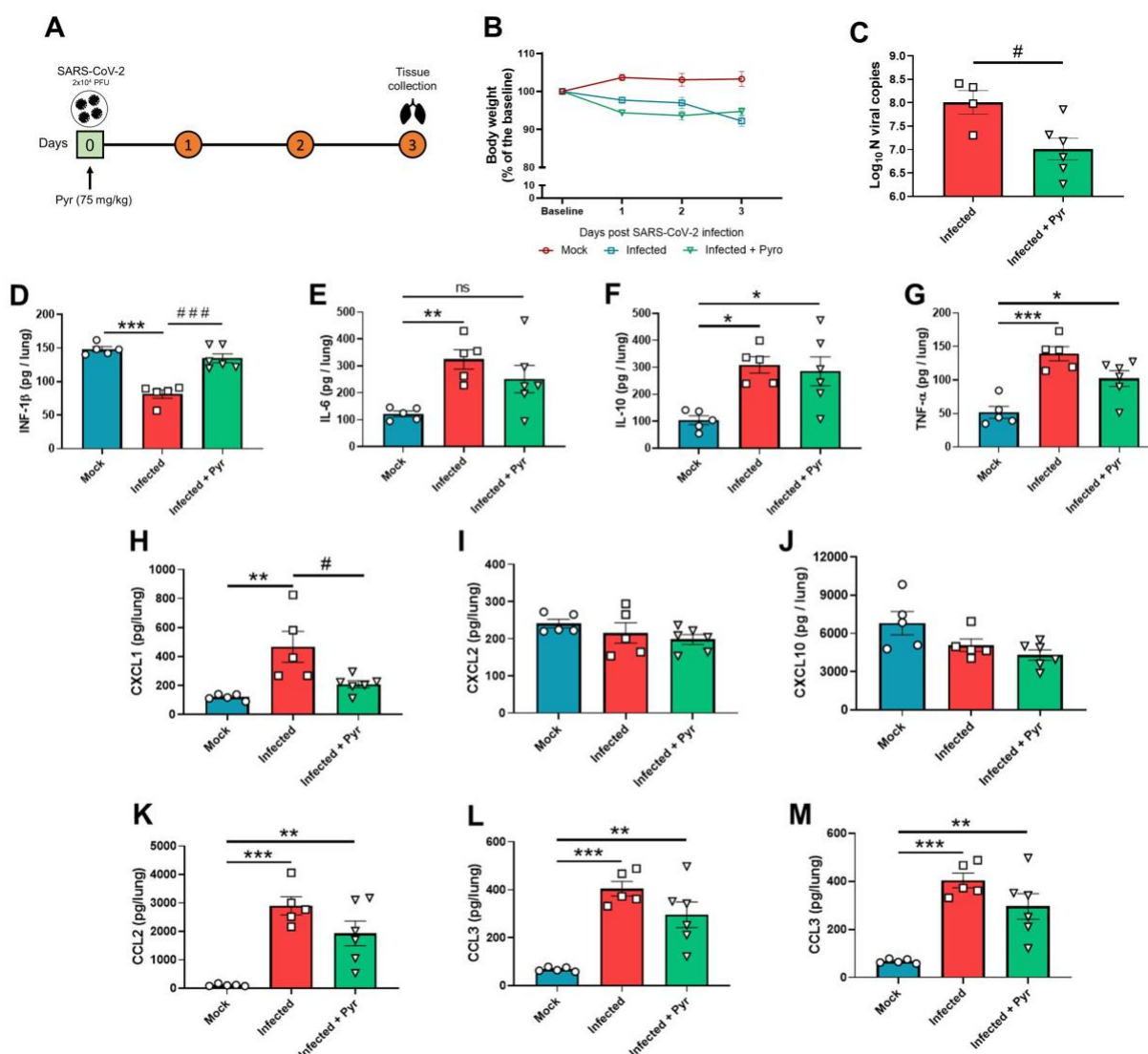


Figure 1: *In vivo* efficacy of pyronaridine in a mouse model of COVID-19. A) Experimental timeline: K18-hACE2 mice were infected with SARS-CoV-2 (2 X 10⁴ PFU/40 μ L saline, intranasal) or mock. One group of mice was treated with pyronaridine (75 mg/kg i.p.) 1 h before virus inoculation. B) Body weight was evaluated daily. C) At 3 DPI, mice were euthanized and the lung viral load, and D-M) Lung cytokines and chemokines levels were determined. * $p < 0.05$, ** $p < 0.01$, and *** $p < 0.001$ as compared with mock group after one-way ANOVA followed by Tukey post-hoc test. # $p < 0.05$ as compared with infected group after one-way ANOVA followed by Tukey post-hoc test. Pyr – Pyronaridine.

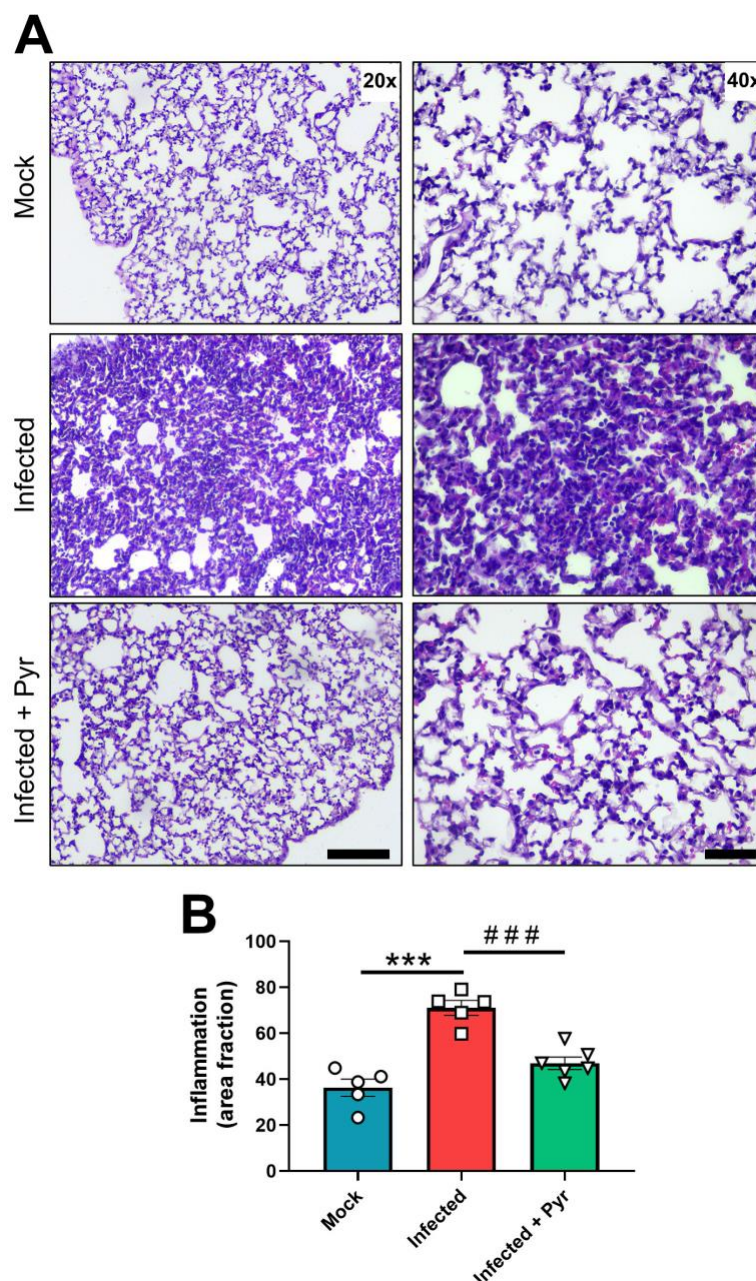


Figure 2: Lung histopathological analyses of COVID-19 mice treated with pyronaridine. K18-hACE2 mice were infected with SARS-CoV-2 (2×10^4 PFU/40 μ L, intranasal) or mock. One group of mice was treated with pyronaridine (75 mg/kg i.p.) 1 h before virus inoculation. At 3 DPI, mice were euthanized, and the lungs were harvested and processed for histopathological analyses. A - Representative images of lung slices stained with hematoxylin and eosin (H&E). B- Quantitative morphometric analyses. *** $p < 0.001$ as compared with mock group after one-way ANOVA followed by Tukey post-hoc test. # $p < 0.05$ and ## $p < 0.01$ as compared with infected group after one-way ANOVA followed by Tukey post-hoc test. Pyr – Pyronaridine. Scale bars: 20X = 125 μ m; 40X = 50 μ m.

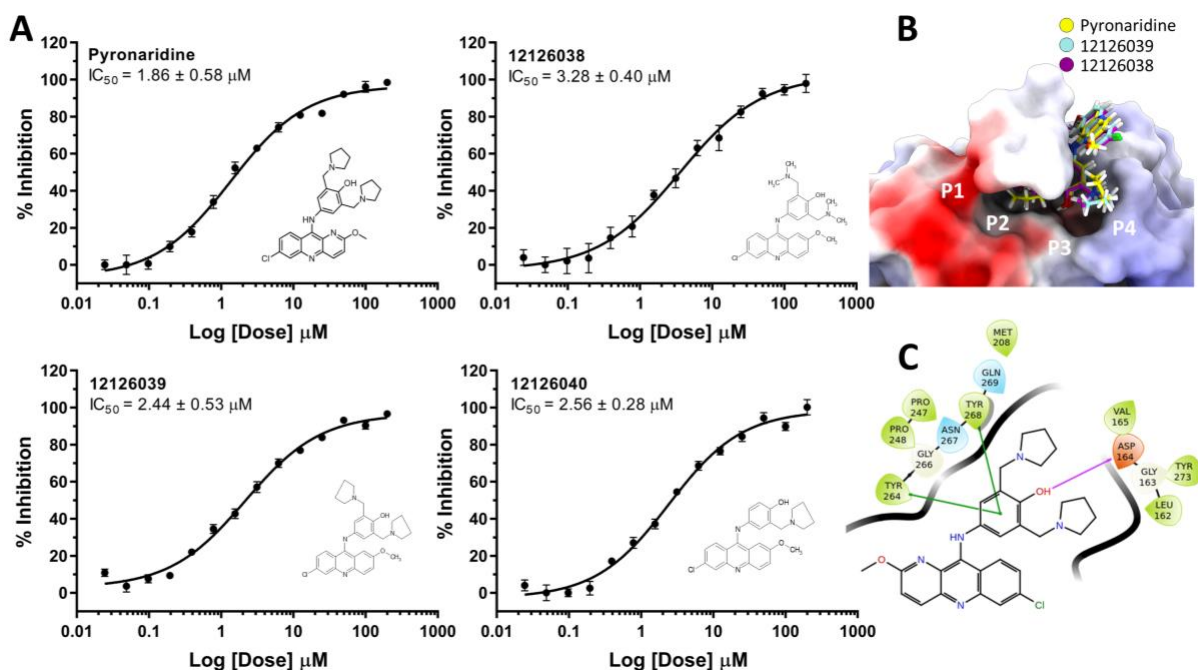


Figure 3 A. Dose-response curves of pyronaridine and active analogs against SARS-CoV-2 PL^{pro}. B. Docking pose of pyronaridine (yellow) and analogs 12126039 (blue) and 12126038 (purple) in PL^{pro} active site (PDB 7JRN). Electrostatic potential projected as surface charge. C. 2D ligand interaction diagram. Hydrogen bonds are depicted in pink, while pi-stackings are depicted in green.

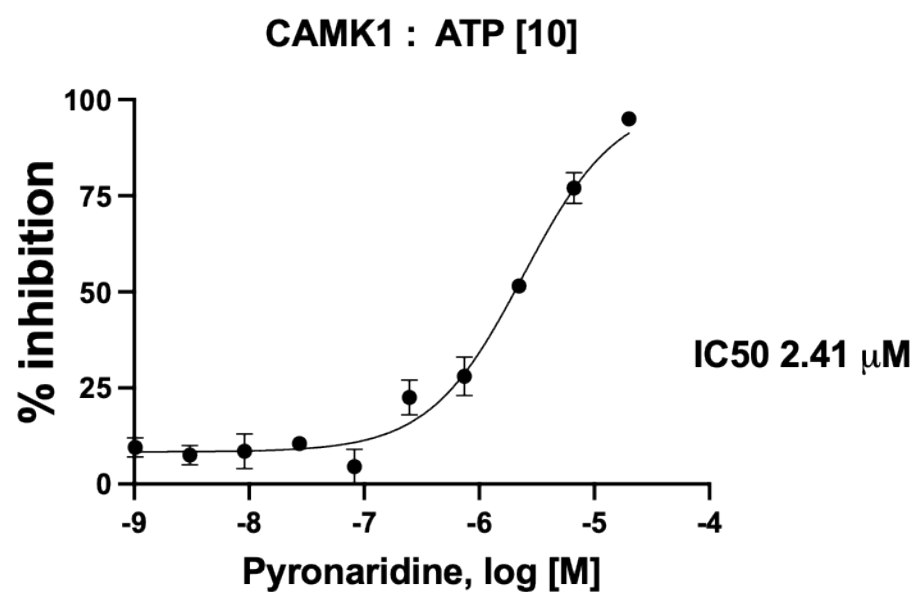
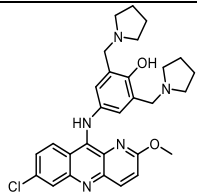
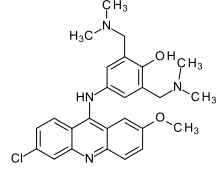
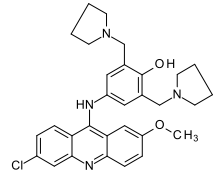
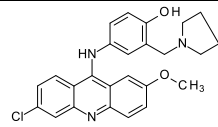
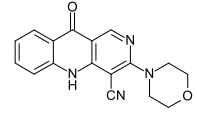
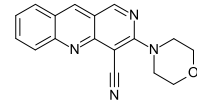
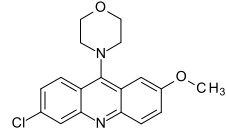
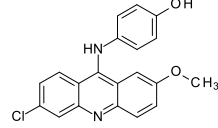
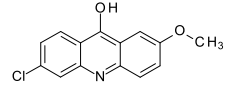


Figure 4: Pyronaridine CAMK1 dose response.

Table 1. PI^{pro} IC₅₀ inhibition data for pyronaridine analogs.

Molecule	Structure	Mol wt	IC ₅₀ (μM)
Pyronaridine		518.05	1.86 ± 0.58
12126038		465.00	3.28 ± 0.4
12126039		517.08	2.44 ± 0.53
12126040		433.94	2.56 ± 0.28
10326099		306.33	>20
12126035		290.33	>20
12126036		328.80	>20
12126037		350.81	>20
12126072		259.69	>20

Materials and Methods

Chemicals and reagents

Pyronaridine tetraphosphate [4-[(7-Chloro-2-methoxybenzo[b][1,5]naphthyridin-10-yl)amino]-2,6-bis(1-pyrrolidinylmethyl)phenol phosphate (1:4)] (12) was purchased from BOC Sciences (Shirley NY). The purity of this compound was greater than 95%. For pyronaridine analogs, ^1H and ^{13}C Spectra were measured on Bruker AC-300 (300 MHz, ^1H) or Bruker AC-200 (50 MHz, ^{13}C). Chemical shifts were measured in DMSO- d_6 or CDCl_3 , using tetramethylsilane as an internal standard, and reported as units (ppm) values. The following abbreviations are used to indicate the multiplicity: s, singlet; d, doublet; t, triplet; m, multiplet; dd, doublet of doublets; brs, broad singlet; brm, broad multiplet. The purity of the final compounds was analyzed on Agilent 1290 Infinity II HPLC system coupled to Agilent 6460 triple-quadrupole mass spectrometer equipped with an electrospray ionization source. The chromatographic separation was carried out on Agilent Eclipse Plus C18 RRHD column (2.1 \times 50 mm, 1.8 μm) at 40 $^\circ\text{C}$, sample injection volume was 0.2 μL . The mobile phase comprising 0.1 % formic acid / water (A), and 0.1 % formic acid and 85 % acetonitrile / water (B) was programmed with gradient elution (0.0-3.0 min, 60 % B; 3.0-4.0 min, 60 % to 97 % B; 4.0-6.0 min, 97 % B; 6.0-6.1 min, 97 % to 60 % B) at a flow rate of 0.4 mL/min. The mass spectrometric detection was operated in positive ion mode. Optimal parameters were: capillary voltages of 3500 V, a nebulizer pressure of 35 psi, a gas temperature of 350 $^\circ\text{C}$, a gas flow rate of 12 L/min. All final compounds are > 95 % pure. Melting points were determined on Electrothermal 9001 (10 $^\circ\text{C}$ per min) and are uncorrected. Merck KGaA silica gel 60 F₂₅₄ plates were used for

analytical thin-layer chromatography. Column chromatography was performed on Merck silica gel 60 (70-230 mesh). Yields refer to purified products and are not optimized.

The molecules were synthesized according to Scheme 1 or Scheme 2 and the specific methods and analytical results are described in the Supplemental Methods.

Test Article Preparation

Dose formulation for pyronaridine was prepared as previously described (13) under yellow light by mixing the appropriate amount of pyronaridine in melted Kolliphor HS 15 (Solutol) (20% final volume) using a vortex mixer for 30 s. The remaining sterile water (Gibco) was added, and the formulations were mixed using a vortex mixer for 30 sec – 5 min until the compound was visually dissolved and then sonication for 25 min. The final 20% Kolliphor HS 15 dose formulations was observed to be a clear, reddish solutions.

Mouse studies

Ethical approval

All the experimental procedures were performed in accordance with the guide for the use of laboratory animals of the University of Sao Paulo and approved by the institutional ethics committee under the protocol number 105/2021.

SARS-CoV-2 isolate

SARS-CoV-2 was isolated from a COVID-19 positive-tested patient. The virus was propagated and titrated in Vero E6 cells in a biosafety level 3 laboratory (BSL3) at the

Ribeirão Preto Medical school (Ribeirão Preto, Brazil). Cells were cultured in DMEM medium supplemented with 10% fetal bovine serum (FBS) and antibiotic/antimycotic (Penicillin 10,000 U/mL; Streptomycin 10,000 µg/mL). The viral inoculum was added to Vero cells in DMEM 2% FBS and incubated at 37 °C with 5% CO₂ for 48 h. The cytopathogenic effect (CPE) was observed under a microscope. Cell monolayer was collected, and the supernatant was stored in -70 °C. Virus titration was made by the plaque-forming units (PFU).

K18-hACE2 mice

To evaluate the effects of Pyronaridine *in vivo*, we infected the K18-hACE2 humanized mice (B6.Cg-Tg(K18-ACE2)2PrImn/J)(21, 65, 66). K18-hACE2 mice were obtained from The Jackson Laboratory and were breed in the Centro de Criação de Animais Especiais (Ribeirão Preto Medical School/University of São Paulo). This mouse model for SARS-CoV-2-induced disease has been used as it presents clinical signs, and biochemical and histopathological changes compatible with the human disease(65-71). Mice had access to water and food *ad libitum*. For the experimental infection, animals were transferred to the BSL3 facility.

SARS-CoV-2 experimental infection and treatments

Female K18-hACE2 mice, 8-week-old, were infected with 2x10⁴ PFU of SARS-CoV-2 (in 40 µL) by intranasal route. Uninfected mice (N = 5) were inoculated with equal volume of PBS (Phosphate buffered saline - 137 mM NaCl, 2.7 mM KCl, 10 mM Na₂HPO₄, 1.8 mM KH₂PO₄; pH 7.4). On the day of infection, 1 h before virus inoculation, animals were

treated with Pyronaridine (75 mg/kg, i.p.) (n = 6). Five infected animals remained untreated. Body weight was evaluated on the baseline and on all the days post-infection. On the day 3 post-infection animals were humanely euthanized, and lungs were collected. Right lung was collected, harvested, and homogenized in PBS with steel glass beads. The homogenate was added to TRIzol® (Invitrogen, CA, EUA) reagent (1:1), for posterior viral titration via RT-qPCR, or to lysis buffer (1:1), for ELISA assay, and stored at -70 °C. The left lung was collected in paraformaldehyde (PFA 4%) for posterior histological assessment.

Absolute viral copies quantification

Total RNA from the right lungs were obtained using the Trizol® (Invitrogen, CA, EUA) method and quantified using NanoDrop One/OneC (ThermoFisher Scientific, USA). A total of 800 ng of RNA was used to synthesize cDNA using the High-Capacity cDNA Reverse Transcription kit (Applied Biosystems, Foster City, CA, USA), following the manufacturer's protocol. The determination of the absolute number of viral copies was made by a Taqman real-time qPCR assay with the aid of the StepOne™ Real-Time PCR System (Applied Biosystems, Foster City, CA, USA). A standard curve was generated in order to obtain the exact number of copies in the tested sample, using an amplicon containing 944 bp cloned from a plasmid (PTZ57R/T CloneJet™ Cloning Kit Thermo Fisher®), starting in the nucleotide 14 of the gene N. To quantify the number of copies, a serial dilution of the plasmid in the proportion of 1:10 was performed. Commercial primers and probes for the N1 gene and RNase P (endogenous control) were used for the quantification (2019-nCov CDC EUA Kit, IDT), following the CDC's instructions.

ELISA assay

Lung homogenate was added to RIPA buffer (Radioimmunoprecipitation assay buffer – 150 mM NaCl, 1% NP-40 or Triton X-100, 0.5% sodium deoxycholate, 0.1% SDS, 50 mM Tris; pH 8.0) in proportion of 1:1, and then centrifuged at 10,000 x *g* at 4 °C for 10 min. Supernatant was collected and stored in -70 °C until use. The Sandwich ELISA method was performed to detect the concentration of cytokines and chemokines using kits from R&D Systems (DuoSet), according to the manufacturer's protocols. The following targets were evaluated: IL-6, IL-10, TNF- α , INF-1 β , CCL2, CCL3, CCL4, CXCL1, CXCL2, and CXCL10.

Lung histopathological process and analyses

Five micrometer lung slices were submitted to Hematoxylin and Eosin staining. A total of 10 photomicrographs in 40X magnification per animal were randomly obtained using a microscope Novel (Novel L3000 LED, China) coupled to a HDI camera for images capture. The total septal area and total area were analyzed with the aid of the Pro Plus 7 software (Media Cybernetics, Inc., MD, USA). Morphometric analysis was performed in accordance with the protocol established by the American Thoracic Society and European Thoracic Society (ATS/ERS) (72).

Synthesis of pyronaridine analogs

All reagents and solvents were purchased from commercial suppliers and used without further purification. ^1H and ^{13}C Spectra were measured on Bruker AC-300 (300 MHz, ^1H)

or Bruker AC-200 (50 MHz, ^{13}C). Chemical shifts were measured in DMSO- d_6 or CDCl_3 , using tetramethylsilane as an internal standard, and reported as units (ppm) values. The following abbreviations are used to indicate the multiplicity: s, singlet; d, doublet; t, triplet; m, multiplet; dd, doublet of doublets; brs, broad singlet; brm, broad multiplet.

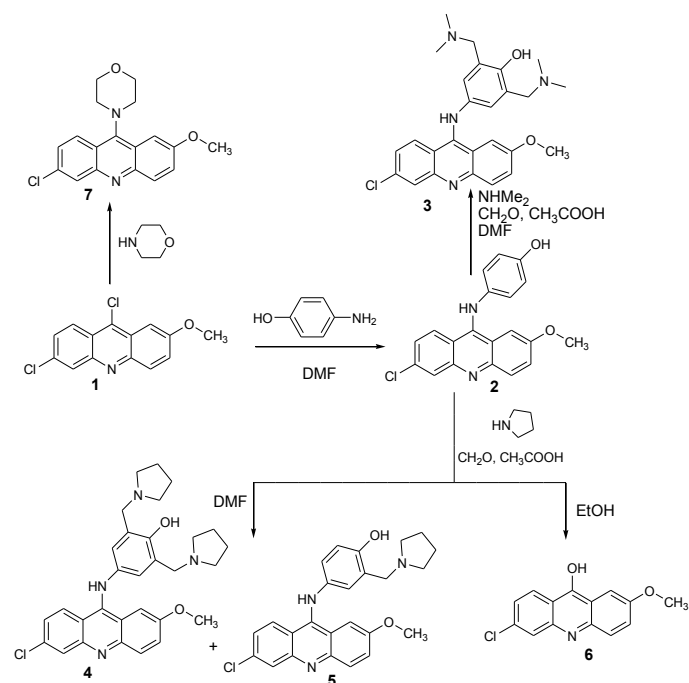
The purity of the final compounds was analyzed on Agilent 1290 Infinity II HPLC system coupled to Agilent 6460 triple-quadrupole mass spectrometer equipped with an electrospray ionization source. The chromatographic separation was carried out on Agilent Eclipse Plus C18 RRHD column (2.1 \times 50 mm, 1.8 μm) at 40 $^\circ\text{C}$, sample injection volume was 0.2 μL . The mobile phase comprising 0.1 % formic acid / water (A), and 0.1 % formic acid and 85 % acetonitrile / water (B) was programmed with gradient elution (0.0-3.0 min, 60 % B; 3.0-4.0 min, 60 % to 97 % B; 4.0-6.0 min, 97 % B; 6.0-6.1 min, 97 % to 60 % B) at a flow rate of 0.4 mL/min. The mass spectrometric detection was operated in positive ion mode. Optimal parameters were: capillary voltages of 3500 V, a nebulizer pressure of 35 psi, a gas temperature of 350 $^\circ\text{C}$, a gas flow rate of 12 L/min. All final compounds are > 95 % pure. Melting points were determined on Electrothermal 9001 (10 $^\circ\text{C}$ per min) and are uncorrected. Merck KGaA silica gel 60 F₂₅₄ plates were used for analytical thin-layer chromatography. Column chromatography was performed on Merck silica gel 60 (70-230 mesh). Yields refer to purified products and are not optimized. The molecules were synthesized according to Scheme 1 or Scheme 2 and the specific methods and analytical results are described in the Supplemental Methods.

Molecular docking

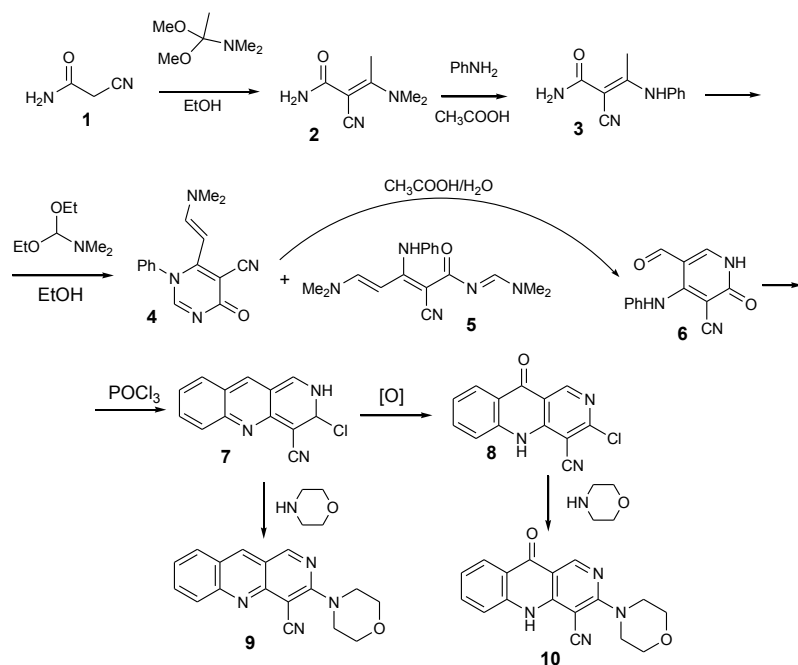
Molecular docking was performed using Glide software (Schrödinger, 2017, USA) and the SARS-CoV-2 PL^{pro} X-ray structure was downloaded from the Protein Data Bank (PDBid 7JRN). Prior to docking, ligand and protein were prepared with LigPrep (Schrödinger, 2017, USA) and Protein Preparation Wizard (Schrödinger, 2017, USA) using default parameters. Different grids were generated with Receptor Grid Generation at possible sites founded in SiteMap (Schrödinger, 2017, USA). Pyronaridine and studied analogs were docked at all sites using Glide in extra precision mode (XP mode) with default parameters (73). The site with the highest *gscore* was considered the binding site for each compound. A similar protocol was also performed using Haddock v2.4 (74). Electrostatic potential was calculated with APBS. Figures were generated with ChimeraX.

Molecule synthesis

Scheme 1. Synthetic route for 6-chloro-2-methoxyacridine derivatives



Scheme 2. Synthetic route for benzo[b]-1,6-naphthyridine derivatives



4-[(6-chloro-2-methoxyacridin-9-yl)amino]phenol 2. (12126037)

Solid 2-aminophenol (0.39 g, 3.6 mmol) was added to a suspension of starting 6,9-dichloro-2-methoxyacridine 1 (0.5 g, 1.8 mmol) in 10 ml of dimethylformamide. The reaction mass was stirred at reflux for 1 hour. Cooled, the precipitate was filtered off, wash with DMF, EtOH and diethyl ether. The yield 72%. Mp 290 °C with decomposition, (DMF). Mass (EI), m/z (Irelat. (%)): 350.7981 [M]⁺ (92). C₂₀H₁₅ClN₂O₂. ¹H NMR (DMSO-d₆; δ , ppm): 9.98 (1H, s, NH), 8.16 (3H, m, 3CH), 7.73 (2H, m, 2CH), 7.47 (1H, d, J = 4.5, CH), 7.23 (2H, d, J = 6.5, 2CH), 6.92 (2H, d, J = 6.5, 2CH), 3.81 (3H, s, OCH₃). ¹³C NMR

(DMSO-d₆; δ , ppm): 156.0, 152.9, 147.8, 147.6, 145.1, 144.7, 133.7, 131.3, 131.1, 128.1, 122.8, 121.8, 121.5, 121.4, 120.9, 120.3, 120.1, 117.9, 101.0, 55.7.

4-[(6-chloro-2-methoxyacridin-9-yl)amino]-2,6-bis[(dimethylamino)methyl]phenol

3. (12126038) A mixture of 40% aqueous solution of dimethylamine (1.1 ml, 9.0 mmol), 1 ml of acetic acid and 37% aqueous solution of formaldehyde (0.39 ml, 5.4 mmol) were added at once to a suspension of 4-[(6-chloro-2-methoxyacridin-9-yl)amino]phenol 2 (0.9 mmol) in 10 ml of dimethylformamide. The suspension was heated to boiling and boiled for 4 hours. The reaction mixture was cooled, an aqueous solution of NaHCO₃ (17 mmol) is added, transferred to a separatory funnel and extracted with ethyl acetate (30 ml x 2). Combined organic layer was washed with water 2 x 100 ml and dried over sodium sulfate. The solvent was removed in vacuo and residue oil was treated by mixture of 20 ml of hexane and 1 ml of diethyl ether. The oil was ground and kept for 10 hours at 40 °C. The solid was filtered off, washed with hexane and purified by column chromatography (methanol). The yield of aim product was 25%. Mp 148-152 °C. Mass (EI), m/z ($I_{relat.}(\%)$): 464.9869 [M]⁺ (88). C₂₆H₂₉ClN₄O₂. ¹H NMR (DMSO-d₆; δ , ppm): 9.98 (1H, s, NH), 8.17 (3H, m, 3CH), 7.84 (2H, m, 2CH), 7.45 (1H, d, J = 4.5, CH), 7.06 (2H, s, 2CH), 3.81 (3H, s, OCH₃), 3.61 (2H, s, 2CH₂), 2.78 (12H, br s, 2N(CH₃)₂). ¹³C NMR (DMSO-d₆; δ , ppm): 157.2, 156.0, 154.5, 147.8, 145.1, 144.6, 133.7, 131.3, 131.1, 128.0, 128.1, 125.5, 122.8, 121.4, 118.6, 114.9, 112.2, 101.0, 55.8, 55.7, 44.9.

4-[(6-chloro-2-methoxyacridin-9-yl)amino]-2-(pyrrolidin-1-ylmethyl)phenol 4 and **4-[(6-chloro-2-methoxyacridin-9-yl)amino]-2,6-bis(pyrrolidin-1-ylmethyl)phenol 5.**

A mixture of pyrrolidine (0.52 ml, 6.0 mmol), 0.7 ml of acetic acid, and 37% aqueous formaldehyde solution (0.28 ml, 3.6 mmol) were added to a suspension of 4-[(6-chloro-2-methoxyacridin-9-yl)amino]phenol **2** (0.6 mmol) in 10 ml of dimethylformamide. The solution was stirred at reflux for 1 hour. The reaction mixture was cooled, an aqueous solution of NaHCO₃ (11 mmol) was added and extracted with ethyl acetate (2 x 30 ml). The combined organic layer was washed with water (2 x 100 ml), dried by sodium sulfate and solvent was evaporated in vacuo. The resulting oil was dissolved in chloroform and applied to a chromatography column (chloroform/methanol 9:1) and product **4** was isolated. Pure methanol was used as eluent for separation product **5**.

4-[(6-chloro-2-methoxyacridin-9-yl)amino]-2-(pyrrolidin-1-ylmethyl)phenol **4.**

(12126040) The yield is 5%. Mp 178-182 °C. Mass (EI), *m/z* (*I*_{relat.}(%)): 433.9298 [M]⁺ (76). C₂₅H₂₄ClN₃O₂. ¹H NMR (DMSO-d₆; δ, ppm): 10.21 (1H, s, NH), 8.17 (3H, m, 3CH), 7.81 (2H, m, 2CH), 7.45 (1H, d, *J* = 4.5, CH), 7.06 (2H, s, 2CH), 3.83 (3H, s, OCH₃), 3.60 (2H, s, 2CH₂), 2.5-2.7 (8H, br m, 2N(CH₂)₂), 1.6-1.8 (8H, br m, 2(CH₂)₂). ¹³C NMR (DMSO-d₆; δ, ppm): 157.7, 156.2, 154.5, 147.8, 145.1, 144.3, 133.7, 131.3, 131.1, 125.5, 122.8, 121.4, 118.7, 114.9, 111.5, 101.1, 55.7, 54.1, 52.3, 23.4.

4-[(6-chloro-2-methoxyacridin-9-yl)amino]-2,6-bis(pyrrolidin-1-ylmethyl)phenol **5.**

(12126039) The yield is 10%. Mp 145-150 °C. Mass (EI), *m/z* (*I*_{relat.}(%)): 517.0615 [M]⁺ (79). C₃₀H₃₃ClN₄O₂. ¹H NMR (DMSO-d₆; δ, ppm): 10.04 (1H, s, NH), 8.16 (3H, m, 3CH), 7.79 (2H, m, 2CH), 7.47 (1H, d, *J* = 4.5, CH), 7.06 (1H, d, *J* = 4.5, CH), 6.93 (1H, s, CH), 3.83 (3H, s, OCH₃), 3.60 (2H, s, 2CH₂), 2.5-2.7 (8H, br m, 2N(CH₂)₂), 1.6-1.8 (8H, br m,

2(CH₂)₂). ¹³C NMR (DMSO-d₆; δ, ppm): 156.0, 152.4, 149.3, 147.7, 145.1, 139.2, 131.2, 131.1, 128.7, 124.1, 122.8, 121.2, 120.8, 116.4, 116.1, 112.4, 101.6, 55.8, 51.9, 23.42.

6-chloro-2-methoxyacridin-9-ol 6. (12126072)

The mixture of pyrrolidine (1.0 ml, 13.0 mmol), 1.4 ml of acetic acid and 37% aqueous formaldehyde solution (0.56 ml, 7.8 mmol) were added to a suspension of 4-[(6-chloro-2-methoxyacridin-9-yl)amino]phenol 2 (1.3 mmol) in 10 ml of ethanol. The suspension was boiled for 36 hours. The reaction mixture was cooled, an aqueous solution of NaHCO₃ (2.6 mmol) was added and the precipitate of aim compound was filtered off. The yield is 38%. Mp 300 °C (DMF). Mass (EI), *m/z* (*I*_{relat.}(%)): 259.0615 [M]⁺ (79). C₁₄H₁₀ClNO₂. ¹H NMR (DMSO-d₆; δ, ppm): 8.56 (1H, d, *J* = 9.0, CH), 7.72 (H, s, CH), 7.62 (1H, d, *J* = 4.5, CH), 7.44 (1H, d, *J* = 4.5, CH), 7.27 (1H, s, CH), 7.07 (1H, d, *J* = 9.0, CH), 3.86 (3H, s, OCH₃). ¹³C NMR (DMSO-d₆; δ, ppm): 157.8, 148.2, 147.9, 140.6, 138.0, 136.7, 128.7, 126.9, 125.5, 124.6, 123.3, 102.9, 55.3.

6-chloro-2-methoxy-9-morpholin-4-ylacridine 7. (12126036)

Morpholine (0.23 ml, 2.7 mmol) was added to a suspension of starting 6,9-dichloro-2-methoxyacridine 1 (0.25 g, 0.9 mmol) in 7 ml of dimethylformamide. The reaction mixture was stirred at reflux for 30 min, cooled, formed precipitate was filtered off and washed with dimethylformamide, acetone. The yield is 70%. Mp 208-212 °C (DMF). Mass (EI), *m/z* (*I*_{relat.}(%)): 328.7926 [M]⁺ (74). C₁₈H₁₇ClN₂O₂. ¹H NMR (DMSO-d₆; δ, ppm): 8.56 (1H, d, *J* = 9.0, CH), 7.72 (H, s, CH), 7.62 (1H, d, *J* = 4.5, CH), 7.44 (1H, d, *J* = 4.5, CH), 7.27 (1H, s, CH), 7.07 (1H, d, *J* = 9.0, CH), 3.86 (3H, s, OCH₃). ¹³C NMR (DMSO-d₆; δ, ppm):

155.7, 149.8, 142.6, 134.5, 131.7, 130.9, 130.6, 127.6, 122.4, 119.7, 119.1, 114.8, 100.5, 66.8, 55.7, 50.8.

(2E)-2-cyano-3-(dimethylamino)but-2-enamide 2.

Dimethyl acetal dimethylacetamide (1 ml, 7.2 mmol) was added to a suspension of cyanoacetamide 1 (0.5 g, 6 mmol) in 15 ml of absolute alcohol. The suspension was boiled for 3 hours, cooled, obtained precipitate was filtered off, washed with alcohol and diethyl ether. Aim product 2 was obtained with a yield of 82%. Mp 188-192 °C (isopropanol).

(2E)-3-anilino-2-cyanobut-2-enamide 3.

Aniline (0.45 ml, 5 mmol) was added to a suspension of (2E)-2-cyano-3-(dimethylamino)but-2-enamide 2 (0.3 g, 2 mmol) in acetic acid (4 ml). The suspension was boiled for 3 hours, cooled, acetic acid was removed under vacuum/ The residue was treated by water, formed precipitate was filtered off and washed with water, isopropyl alcohol and diethyl ether. Aim product 3 was obtained with a yield of 87%. Mp 179-182 °C (isopropanol).

A mixture of **6-[(E)-2-(dimethylamino)vinyl]-4-oxo-1-phenyl-1,4-dihydropyrimidine-5-carbonitrile 4** and **(2Z,4E)-3-anilino-2-cyano-5-(dimethylamino)-N-[(1E)-(dimethylamino)methylene]penta-2,4-dienamide 5.**

Dimethylformamide diethyl acetal (1.3 ml, 7.5 mmol) was added to a suspension of (2E)-3-anilino-2-cyanobut-2-enamide 3 (0.6 g, 3 mmol) in 5 ml of absolute ethanol. The dark

red solution was boiled for 6 hours. Part of the solvent was removed under vacuum until a thick suspension was obtained. The precipitate was filtered off, washed with absolute alcohol and dry diethyl ether. A mixture of compounds 4 and 5 was obtained.

4-anilino-5-formyl-2-oxo-1,2-dihydropyridine-3-carbonitrile 6.

A mixture of 6-[(E)-2-(dimethylamino)vinyl]-4-oxo-1-phenyl-1,4-dihydropyrimidine-5-carbonitrile 4 and (2Z,4E)-3-anilino-2-cyano-5-(dimethylamino)-N-[(1E)-(dimethylamino)methylene]penta-2,4-dienamide 5 (5.6 g) is dissolved in 56 ml of 90% acetic acid. A precipitate form after 30 min and reaction mixture was stirred at room temperature for 20 h. The precipitate was filtered off, washed with water, ethyl alcohol and acetone. The yield is 2.3 g of aim product 6. Mp 225-230 °C (with decomposition).

3-chloro-2,3-dihydrobenzo[b]-1,6-naphthyridine-4-carbonitrile 7.

The 4-anilino-5-formyl-2-oxo-1,2-dihydropyridine-3-carbonitrile 6 (2.3 g) was refluxed in phosphorus oxychloride (22 ml) for 1 hour. The reaction mixture was poured onto ice, stirred for 30 min. Formed precipitate was filtered off, washed with water, ethyl alcohol, diethyl ether. Aim product 7 was obtained in 80% yield. Mp 300-304 °C (DMF).

3-chloro-10-oxo-5,10-dihydrobenzo[b]-1,6-naphthyridine-4-carbonitrile 8.

To a suspension of 3-chloro-2,3-dihydrobenzo[b]-1,6-naphthyridine-4-carbonitrile 7 (0.44 g) in 15 ml of acetone was added m-chloroperbenzoic acid 55% (1.45 g) in small portions and refluxed for 9 hours. The reaction mixture was cooled, obtained precipitate was

filtered off and washed with acetone, toluene, acetone. The aim product 8 was obtained with a yield 50%. Mp 305 °C.

3-morpholin-4-ylbenzo[b]-1,6-naphthyridine-4-carbonitrile 9. (12126035)

Morpholine (0.16 ml, 1.8 mmol) was added to a suspension of 3-chloro-2,3-dihydrobenzo[b]-1,6-naphthyridine-4-carbonitrile 7 (0.15 g, 0.6 mmol) in 4 ml of dry dimethylformamide. The solution was boiled for 1 hour. Cooled, poured into 40 ml of water, extracted 2 times with 30 ml of ethyl acetate. The organic fractions were additionally washed with water 2 times. Ethyl acetate was removed under vacuum, ethyl alcohol was added to the dry residue, and the precipitate was filtered off. Washed with diethyl ether. The aim product 9 was obtained with a yield of 78%.Mp 222-225 °C (EtOH:DMF 2:1). Mass (EI), m/z ($I_{relat.}(\%)$): 290.3194 $[M]^+$ (79). $C_{17}H_{14}N_4O$. 1H NMR (DMSO- d_6 ; δ , ppm): 9.46 (1H, s, CH), 9.13 (1H, s, CH), 8.16 (1H, d, $J = 6.5$, CH), 7.91 (1H, s, CH), 7.44 (1H, d, $J = 6.5$, CH), 4.16 (4H, m, $O(CH_2)_2$), 3.78 (4H, m, $N(CH_2)_2$). ^{13}C NMR (DMSO- d_6 ; δ , ppm): 144.9, 143.5, 137.8, 136.4, 136.0, 133.1, 129.5, 128.4, 126.8, 126.1, 114.5, 101.4, 66.7, 53.8.

3-morpholin-4-yl-10-oxo-5,10-dihydrobenzo[b]-1,6-naphthyridine-4-carbonitrile 10. (10326099)

Morpholine (0.14 ml, 1.6 mmol) was added to a solution of 3-chloro-10-oxo-5,10-dihydrobenzo[b]-1,6-naphthyridine-4-carbonitrile 8 (0.2 g, 0.8 mmol) in 5 ml of dry dimethylformamide. Formed suspension was stirred at reflux for 1 hour, cooled, the precipitate was filtered off, washed with dimethylformamide and acetone. Mp 290 °C (из

DMF). The yield is 38%. Mass (EI), m/z ($I_{relat.}(\%)$): 306.3188 $[M]^+$ (68). $C_{17}H_{14}N_4O_2$. 1H NMR (DMSO- d_6 ; δ , ppm): 8.02 (1H, s, CH), 7.91 (1H, d, $J = 6.5$, CH), 7.59 (1H, s, CH), 7.09 (1H, d, $J = 6.5$, CH), 4.08 (4H, m, $O(CH_2)_2$), 3.72 (4H, m, $N(CH_2)_2$). ^{13}C NMR (DMSO- d_6 ; δ , ppm): 182.5, 146.4, 146.1, 139.7, 139.1, 138.7, 137.0, 124.9, 122.7, 118.3, 115.4, 108.8, 94.9, 66.8, 53.7.

PL^{pro} cloning, expression, purification and assays

The viral cDNA template (GenBank MT126808.1) was kindly provided by Dr. Edison Durigon. Amplification of the nucleotide sequence coding for the PL^{pro} domain (residues 1564-1879 of SARSCoV-2) was performed by Polymerase Chain Reaction (PCR) using forward (5'- ATTCCATGGGCGAAGTGAGGACTATTAAGGTGTTTAC -3') and reverse (5'- ATTGCTCGAGTGGTTTTATGGTTGTTGTGTAAC -3') primers, with restriction sites for *NcoI* and *XhoI*. PCR product was digested with *NcoI* and *XhoI* and cloned into pET28a (Novagen) in frame with a C-terminal his-tag coding sequence. *E. coli* BL21 transformed with plasmids were grown in LB to an optical density (OD_{600}) of 0.6 at 37 °C and 200 RPM. Protein expression was induced adding 0.5 mM IPTG and 1 mM Zinc Chloride and grown overnight at 18°. The cell pellet was resuspended in lysis buffer (50 mM Tris, 150 mM NaCl, 10 mM imidazole, 1 mM DTT, pH 8.5), disrupted by sonication and centrifuged at 12,500 rpm for 40 min at 4° C. Protein was isolated from the lysate using 5 mL Ni-NTA resin (Qiagen) pre-equilibrated with lysis buffer and then washed with 15 column volumes (CV) with the same buffer. The his-tagged protein was eluted 4 CV of elution buffer (lysis buffer supplemented with 250 mM imidazole) and further purified by size exclusion

chromatography in a Superdex 200 10/30 (GE Healthcare) equilibrated with 20 mM Tris pH 7.4, 100 mM NaCl, 2 mM DTT.

PL^{pro} inhibition assay was performed using the FRET-based fluorescent peptide substrate Abz-TLKGG↓APIKEDDPS-EDDnp, kindly provided by Dr. Maria Aparecida Juliano (Federal University of São Paulo, Brazil). The assay was standardized with enzyme concentration of 70 nM and 27 μM of fluorescent substrate in PL^{pro} assay buffer (50 mM HEPES pH 7.5, 0.01 % Triton X-100 and 5 mM DTT), at 37°C for 30 min. Activity was measured in the plate reader system Spectramax Gemini EM (Molecular devices), with λ_{ex} = 320 nm and λ_{em} = 420 nm, in presence of different inhibitors and 1% DMSO.

M^{pro} cloning, expression, purification and assays

The M^{pro} cloning is described elsewhere (75). For expression, BL21 cells transformed with plasmid were grown in ZYM-5052 to an OD₆₀₀ of 0.6-0.8 at 37°C and 200 RPM. Protein expression was induced lowering the temperature to 18 °C, cells were then grown for 16h and harvested by centrifugation. The cell pellet was resuspended in lysis buffer (20 mM Tris pH 7.8, 150 mM NaCl, 1 mM DTT), disrupted by sonication and centrifuged at 12,000 x g for 40 min at 4 °C. Uncleaved protein with 6xHisTag were isolated from the lysate using Ni-NTA resin (Qiagen). The flow-through (FT) was then used to purify cleaved protein with ammonium sulfate precipitation. Ammonium sulfate was added into the FT to a final concentration of 1M, incubated on ice for 10 min and centrifuged at 12,000 x g for 30 min at 4 °C. The precipitated protein was resuspended in gel filtration buffer (20 mM Tris pH 7.8, 150 mM NaCl, 1 mM EDTA, 1 mM DTT) and purified by size-exclusion chromatography in a HiLoad 26/100 Superdex 200 column (GE Healthcare)

pre-equilibrated with gel filtration buffer. Afterwards, the protein was buffer exchanged to 20 mM Tris pH 8.0, 1.0 mM DTT and loaded into a Mono-Q 5/50 GL column (GE Healthcare) in the same buffer, and eluted with a linear gradient of a buffer containing 20 mM Tris pH 8.0, 1.0 M NaCl and 1.0 mM DTT. Proteins were concentrated at 1.0 mg/mL, flash-frozen and stored at -80°C for inhibition assays.

M^{pro} inhibition assay was performed using the FRET-based fluorescent peptide substrate DABCYL-KTSAVLQ↓SGFRKM-E(EDANS)-NH₂ (purchased from Genscript). The assay was standardized with enzyme concentration of 140 nM and 30 μM of fluorescent substrate in M^{pro} assay buffer containing (20 mM Tris pH 7.3, 1 mM EDTA, 1 mM DTT), at 37°C for 30 min. Activity was detected in the spectrofluorometer system Spectramax Gemini EM (Molecular devices), with λ_{ex} = 360 nm and λ_{em} 460 nm, in presence of different inhibitors and 1% DMSO.

Kinase profiling of pyronaridine

Kinase profiling was performed for pyronaridine (1 μM) in duplicate by ThermoFisher (Life Technologies Corporation, Chicago, IL 60693) using Z'Lyte (76), Adapta (77) and LanthaScreen (78) assays for 485 purified kinases.

CAMK1 inhibition

Pyronaridine inhibition of CAMK1 was performed by Selected Services (Thermo Fisher) using the Adapta universal kinase assay, which is a homogenous, fluorescent-based immunoassay for the detection of ADP. The 2X CAMK1 (CaMK1) and ZIPtide mixture was prepared in 50 mM HEPES pH 7.5, 0.01% BRIJ-35, 10 mM MgCl₂, 1 mM EGTA, 4

mM CaCl₂, 800 U/ml Calmodulin, 0.02% NaN₃. The final 10 µL Kinase Reaction consists of 0.25 - 1.2 ng CAMK1 (CaMK1) and 200 µM ZIPtide in 32.5 mM HEPES pH 7.5, 0.005% BRIJ-35, 5 mM MgCl₂, 500 µM EGTA, 2 mM CaCl₂, 400 U/ml Calmodulin, 0.01% NaN₃. After the 1 h kinase reaction incubation, 5 µL of Detection Mix is added.

Supplemental Material

Research Article

Pyronaridine Protects Against SARS-CoV-2 in Mouse

Ana C. Puhl^{1*#}, Giovanni F. Gomes^{2*}, Samara Damasceno² Andre S. Godoy³, Gabriela D. Noske³, Aline M. Nakamura³, Victor O. Gawriljuk³, Rafaela S. Fernandes³, Natalia Monakhova⁴, Olga Riabova⁴, Thomas R. Lane¹, Vadim Makarov⁴, Flavio P. Veras², Sabrina S. Batah⁵, Alexandre T. Fabro⁵, Glaucius Oliva³, Fernando Q. Cunha², José C. Alves-Filho^{2#} Thiago M. Cunha^{2#} and Sean Ekins^{1#}.

¹Collaborations Pharmaceuticals, Inc., 840 Main Campus Drive, Lab 3510, Raleigh, NC 27606, USA.

² Center for Research in Inflammatory Diseases (CRID), Ribeirao Preto Medical School, University of Sao Paulo, Avenida Bandeirantes, 3900, Ribeirao Preto, 14049-900 ; Sao Paulo, Brazil.

³ Institute of Physics of Sao Carlos, University of Sao Paulo, Av. Joao Dagnone, 1100 - Jardim Santa Angelina, Sao Carlos, 13563-120, Brazil.

⁴ Research Center of Biotechnology RAS, 119071 Moscow, Russia.

⁵ Department of Pathology and Legal Medicine, Ribeirão Preto Medical School, University of São Paulo, Ribeirão Preto, Brazil.

* Both authors contribute equally

#To whom correspondence should be addressed: Ana C. Puhl, E-mail address: ana@collaborationspharma.com; Thiago M. Cunha E-mail address: thicunha@fmrp.usp.br; Sean Ekins, E-mail address: sean@collaborationspharma.com,

Short running title: Pyronaridine *in-vivo* efficacy against SARS-CoV-2

Table S1.

SelectScreen kinase profiling of pyronaridine at 1 μ M tested in duplicate.

Kinase	% inhibition mean	assay
CAMK1 (CaMK1)	35	Adapta
CDK4/cyclin D1	1	Adapta
CDK4/cyclin D3	-6	Adapta
CDK6/cyclin D1	1	Adapta
CDK7/cyclin H/MNAT1	-13	Adapta
CDK9/cyclin T1	5	Adapta
CHUK (IKK alpha)	0	Adapta
DAPK1	11	Adapta
GSG2 (Haspin)	9	Adapta
IRAK1	-4	Adapta
LRRK2 FL	-4	Adapta
LRRK2 G2019S FL	-10	Adapta
LRRK2 G2019S	4	Adapta
LRRK2 I2020T	-15	Adapta
LRRK2 R1441C	-7	Adapta
LRRK2	-2	Adapta
NUAK1 (ARK5)	11	Adapta
PI4K2A (PI4K2 alpha)	4	Adapta
PI4K2B (PI4K2 beta)	2	Adapta
PI4KA (PI4K alpha)	0	Adapta
PI4KB (PI4K beta)	5	Adapta
PIK3C2A (PI3K-C2 alpha)	-1	Adapta
PIK3C2B (PI3K-C2 beta)	-5	Adapta
PIK3C2G (PI3K-C2 gamma)	3	Adapta
PIK3C3 (hVPS34)	-4	Adapta
PIK3CA E542K/PIK3R1 (p110 alpha E542K/p85 alpha)	-4	Adapta
PIK3CA E545K/PIK3R1 (p110 alpha E545K/p85 alpha)	3	Adapta
PIK3CA/PIK3R1 (p110 alpha/p85 alpha)	7	Adapta
PIK3CA/PIK3R3 (p110 alpha/p55 gamma)	1	Adapta
PIK3CB/PIK3R1 (p110 beta/p85 alpha)	-11	Adapta
PIK3CB/PIK3R2 (p110 beta/p85 beta)	-2	Adapta
PIK3CD/PIK3R1 (p110 delta/p85 alpha)	9	Adapta

PIK3CG (p110 gamma)	2	Adapta
PIP4K2A	15	Adapta
PIP5K1A	-6	Adapta
PIP5K1B	-11	Adapta
PIP5K1C	-3	Adapta
SPHK1	10	Adapta
SPHK2	-5	Adapta
<hr/>		
AAK1	0	Lanthascreen
ABL1 H396P	7	Lanthascreen
ABL1 M351T	8	Lanthascreen
ABL1 Q252H	-10	Lanthascreen
ACVR1 (ALK2) R206H	2	Lanthascreen
ACVR1 (ALK2)	0	Lanthascreen
ACVR2A	-6	Lanthascreen
ACVR2B	8	Lanthascreen
ACVRL1 (ALK1)	12	Lanthascreen
ADCK3	-16	Lanthascreen
ALK C1156Y	-2	Lanthascreen
ALK F1174L	8	Lanthascreen
ALK L1196M	-3	Lanthascreen
ALK R1275Q	6	Lanthascreen
ALK T1151_L1152insT	4	Lanthascreen
AMPK (A1/B1/G2)	-7	Lanthascreen
AMPK (A1/B1/G3)	-1	Lanthascreen
AMPK (A1/B2/G1)	-2	Lanthascreen
AMPK (A2/B2/G1)	6	Lanthascreen
AMPK (A2/B2/G2)	3	Lanthascreen
ANKK1	-2	Lanthascreen
AXL R499C	3	Lanthascreen
BMPR1A (ALK3)	10	Lanthascreen
BMPR1B (ALK6)	-3	Lanthascreen
BMPR2	8	Lanthascreen
BRAF V599E	4	Lanthascreen
BRAF	-11	Lanthascreen
BRSK2	4	Lanthascreen
CAMK2G (CaMKII gamma)	-1	Lanthascreen
CAMKK1 (CAMKKA)	15	Lanthascreen
CAMKK2 (CaMKK beta)	-1	Lanthascreen
CASK	2	Lanthascreen
CDC7/DBF4	-6	Lanthascreen

CDK11 (Inactive)	-1	Lanthascreen
CDK11/cyclin C	-18	Lanthascreen
CDK13/cyclin K	-13	Lanthascreen
CDK14 (PFTK1)/cyclin Y	14	Lanthascreen
CDK16 (PCTK1)/cyclin Y	-12	Lanthascreen
CDK2/cyclin A1	5	Lanthascreen
CDK2/cyclin E1	0	Lanthascreen
CDK2/cyclin O	2	Lanthascreen
CDK3/cyclin E1	3	Lanthascreen
CDK5 (Inactive)	-1	Lanthascreen
CDK8/cyclin C	3	Lanthascreen
CDK9 (Inactive)	-10	Lanthascreen
CDK9/cyclin K	5	Lanthascreen
CLK4	6	Lanthascreen
DAPK2	-6	Lanthascreen
DDR1	-2	Lanthascreen
DDR2 N456S	17	Lanthascreen
DDR2 T654M	-11	Lanthascreen
DDR2	0	Lanthascreen
DMPK	4	Lanthascreen
DYRK2	-7	Lanthascreen
EGFR (ErbB1) d746-750	-10	Lanthascreen
EGFR (ErbB1) d747-749 A750P	0	Lanthascreen
EIF2AK2 (PKR)	4	Lanthascreen
EPHA3	11	Lanthascreen
EPHA6	-3	Lanthascreen
EPHA7	-3	Lanthascreen
ERN1	6	Lanthascreen
ERN2	6	Lanthascreen
FGFR1 V561M	5	Lanthascreen
FGFR3 G697C	7	Lanthascreen
FGFR3 K650M	-4	Lanthascreen
FLT3 ITD	9	Lanthascreen
FYN A	-3	Lanthascreen
GAK	28	Lanthascreen
GRK1	1	Lanthascreen
HUNK	-1	Lanthascreen
ICK	0	Lanthascreen
IRAK3	-5	Lanthascreen
KIT A829P	-9	Lanthascreen

KIT D816H	-7	Lanthascreen
KIT D816V	-3	Lanthascreen
KIT D820E	-4	Lanthascreen
KIT N822K	14	Lanthascreen
KIT T670E	1	Lanthascreen
KIT V559D T670I	-10	Lanthascreen
KIT V654A	10	Lanthascreen
KIT Y823D	-4	Lanthascreen
LATS2	-4	Lanthascreen
LIMK1	-7	Lanthascreen
LIMK2	-1	Lanthascreen
MAP2K1 (MEK1) S218D S222D	3	Lanthascreen
MAP2K1 (MEK1)	1	Lanthascreen
MAP2K2 (MEK2)	-3	Lanthascreen
MAP2K4 (MEK4)	1	Lanthascreen
MAP2K5 (MEK5)	1	Lanthascreen
MAP2K6 (MKK6) S207E T211E	10	Lanthascreen
MAP2K6 (MKK6)	9	Lanthascreen
MAP3K10 (MLK2)	0	Lanthascreen
MAP3K11 (MLK3)	2	Lanthascreen
MAP3K14 (NIK)	2	Lanthascreen
MAP3K2 (MEKK2)	7	Lanthascreen
MAP3K3 (MEKK3)	-3	Lanthascreen
MAP3K5 (ASK1)	-11	Lanthascreen
MAP3K7/MAP3K7IP1 (TAK1-TAB1)	1	Lanthascreen
MAP4K1 (HPK1)	1	Lanthascreen
MAP4K3 (GLK)	1	Lanthascreen
MAPK10 (JNK3)	5	Lanthascreen
MAPK15 (ERK7)	-11	Lanthascreen
MAPK8 (JNK1)	3	Lanthascreen
MAPK9 (JNK2)	6	Lanthascreen
MASTL	3	Lanthascreen
MERTK (cMER) A708S	0	Lanthascreen
MET D1228H	3	Lanthascreen
MKNK2 (MNK2)	2	Lanthascreen
MLCK (MLCK2)	-6	Lanthascreen
MLK4	8	Lanthascreen
MYLK (MLCK)	4	Lanthascreen
MYLK4	-9	Lanthascreen
MYO3A (MYO3 alpha)	-6	Lanthascreen

MYO3B (MYO3 beta)	5	Lanthascreen
NEK8	0	Lanthascreen
NLK	8	Lanthascreen
NUAK2	2	Lanthascreen
PKMYT1	1	Lanthascreen
PKN2 (PRK2)	6	Lanthascreen
PLK4	6	Lanthascreen
PRKACB (PRKAC beta)	12	Lanthascreen
PRKACG (PRKAC gamma)	2	Lanthascreen
RAF1 (cRAF) Y340D Y341D	-5	Lanthascreen
RET G691S	-3	Lanthascreen
RET M918T	-3	Lanthascreen
RET V804M	-1	Lanthascreen
RIPK2	1	Lanthascreen
RIPK3	-7	Lanthascreen
SIK1	2	Lanthascreen
SIK3	-2	Lanthascreen
SLK	-1	Lanthascreen
STK16 (PKL12)	5	Lanthascreen
STK17A (DRAK1)	1	Lanthascreen
STK17B (DRAK2)	-4	Lanthascreen
STK32B (YANK2)	0	Lanthascreen
STK32C (YANK3)	1	Lanthascreen
STK33	11	Lanthascreen
STK38 (NDR)	2	Lanthascreen
STK38L (NDR2)	-7	Lanthascreen
STK39 (STLK3)	-19	Lanthascreen
TAOK1	-4	Lanthascreen
TAOK3 (JIK)	-2	Lanthascreen
TEC	7	Lanthascreen
TEK (TIE2) R849W	-3	Lanthascreen
TEK (TIE2) Y1108F	-2	Lanthascreen
TESK1	-2	Lanthascreen
TESK2	-3	Lanthascreen
TGFBR1 (ALK5)	-4	Lanthascreen
TGFBR2	-4	Lanthascreen
TLK1	12	Lanthascreen
TLK2	-2	Lanthascreen
TNIK	-1	Lanthascreen
TNK2 (ACK)	1	Lanthascreen

TTK	4	Lanthascreen
ULK1	-4	Lanthascreen
ULK2	2	Lanthascreen
ULK3	8	Lanthascreen
VRK2	-4	Lanthascreen
WEE1	10	Lanthascreen
WNK1	4	Lanthascreen
WNK2	4	Lanthascreen
WNK3	7	Lanthascreen
ZAK	0	Lanthascreen
ABL1 E255K	7	Z'Lyte
ABL1 F317I	0	Z'Lyte
ABL1 F317L	-1	Z'Lyte
ABL1 G250E	1	Z'Lyte
ABL1 T315I	11	Z'Lyte
ABL1 Y253F	-1	Z'Lyte
ABL1	2	Z'Lyte
ABL2 (Arg)	2	Z'Lyte
ACVR1B (ALK4)	-1	Z'Lyte
ADRBK1 (GRK2)	-3	Z'Lyte
ADRBK2 (GRK3)	-5	Z'Lyte
AKT1 (PKB alpha)	4	Z'Lyte
AKT2 (PKB beta)	1	Z'Lyte
AKT3 (PKB gamma)	7	Z'Lyte
ALK	-1	Z'Lyte
AMPK (A1/B2/G2)	-2	Z'Lyte
AMPK (A1/B2/G3)	4	Z'Lyte
AMPK (A2/B1/G2)	1	Z'Lyte
AMPK (A2/B1/G3)	2	Z'Lyte
AMPK (A2/B2/G3)	2	Z'Lyte
AMPK A1/B1/G1	5	Z'Lyte
AMPK A2/B1/G1	2	Z'Lyte
AURKA (Aurora A)	9	Z'Lyte
AURKB (Aurora B)	5	Z'Lyte
AURKC (Aurora C)	-11	Z'Lyte
AXL	1	Z'Lyte
BLK	3	Z'Lyte
BMX	11	Z'Lyte
BRAF V599E	0	Z'Lyte
BRAF	4	Z'Lyte

BRSK1 (SAD1)	2	Z'Lyte
BTK	9	Z'Lyte
CAMK1D (CaMKI delta)	-26	Z'Lyte
CAMK1G (CAMKI gamma)	0	Z'Lyte
CAMK2A (CaMKII alpha)	4	Z'Lyte
CAMK2B (CaMKII beta)	1	Z'Lyte
CAMK2D (CaMKII delta)	-5	Z'Lyte
CAMK4 (CaMKIV)	-5	Z'Lyte
CDC42 BPA (MRCKA)	2	Z'Lyte
CDC42 BPB (MRCKB)	-3	Z'Lyte
CDC42 BPG (MRCKG)	1	Z'Lyte
CDK1/cyclin B	5	Z'Lyte
CDK17/cyclin Y	-2	Z'Lyte
CDK18/cyclin Y	1	Z'Lyte
CDK2/cyclin A	0	Z'Lyte
CDK5/p25	0	Z'Lyte
CDK5/p35	3	Z'Lyte
CDKL5	4	Z'Lyte
CHEK1 (CHK1)	8	Z'Lyte
CHEK2 (CHK2)	0	Z'Lyte
CLK1	-1	Z'Lyte
CLK2	3	Z'Lyte
CLK3	-3	Z'Lyte
CSF1R (FMS)	-3	Z'Lyte
CSK	-3	Z'Lyte
CSNK1A1 (CK1 alpha 1)	5	Z'Lyte
CSNK1A1L	3	Z'Lyte
CSNK1D (CK1 delta)	5	Z'Lyte
CSNK1E (CK1 epsilon) R178C	1	Z'Lyte
CSNK1E (CK1 epsilon)	1	Z'Lyte
CSNK1G1 (CK1 gamma 1)	0	Z'Lyte
CSNK1G2 (CK1 gamma 2)	4	Z'Lyte
CSNK1G3 (CK1 gamma 3)	2	Z'Lyte
CSNK2A1 (CK2 alpha 1)	7	Z'Lyte
CSNK2A2 (CK2 alpha 2)	5	Z'Lyte
DAPK3 (ZIPK)	2	Z'Lyte
DCAMKL1 (DCLK1)	0	Z'Lyte
DCAMKL2 (DCK2)	-1	Z'Lyte
DNA-PK	5	Z'Lyte
DYRK1A	3	Z'Lyte

DYRK1B	1	Z'Lyte
DYRK3	1	Z'Lyte
DYRK4	0	Z'Lyte
EEF2K	1	Z'Lyte
EGFR (ErbB1) C797S	-7	Z'Lyte
EGFR (ErbB1) G719C	-4	Z'Lyte
EGFR (ErbB1) G719S	-5	Z'Lyte
EGFR (ErbB1) L858R	5	Z'Lyte
EGFR (ErbB1) L861Q	-4	Z'Lyte
EGFR (ErbB1) T790M C797S L858R	2	Z'Lyte
EGFR (ErbB1) T790M L858R	5	Z'Lyte
EGFR (ErbB1) T790M	2	Z'Lyte
EGFR (ErbB1)	-5	Z'Lyte
EPHA1	1	Z'Lyte
EPHA2	5	Z'Lyte
EPHA4	-2	Z'Lyte
EPHA5	-3	Z'Lyte
EPHA8	1	Z'Lyte
EPHB1	2	Z'Lyte
EPHB2	4	Z'Lyte
EPHB3	-1	Z'Lyte
EPHB4	7	Z'Lyte
ERBB2 (HER2)	2	Z'Lyte
ERBB4 (HER4)	-2	Z'Lyte
FER	-21	Z'Lyte
FES (FPS)	-10	Z'Lyte
FGFR1	-5	Z'Lyte
FGFR2 N549H	2	Z'Lyte
FGFR2	-1	Z'Lyte
FGFR3 K650E	-4	Z'Lyte
FGFR3 V555M	-1	Z'Lyte
FGFR3	-2	Z'Lyte
FGFR4	-14	Z'Lyte
FGR	11	Z'Lyte
FLT1 (VEGFR1)	-6	Z'Lyte
FLT3 D835Y	2	Z'Lyte
FLT3	3	Z'Lyte
FLT4 (VEGFR3)	3	Z'Lyte
FRAP1 (mTOR)	1	Z'Lyte
FRK (PTK5)	-2	Z'Lyte

FYN	2	Z'Lyte
GRK4	25	Z'Lyte
GRK5	10	Z'Lyte
GRK6	-1	Z'Lyte
GRK7	4	Z'Lyte
GSK3A (GSK3 alpha)	4	Z'Lyte
GSK3B (GSK3 beta)	8	Z'Lyte
HCK	4	Z'Lyte
HIPK1 (Myak)	1	Z'Lyte
HIPK2	-1	Z'Lyte
HIPK3 (YAK1)	-2	Z'Lyte
HIPK4	5	Z'Lyte
IGF1R	6	Z'Lyte
IKBKB (IKK beta)	1	Z'Lyte
IKBKE (IKK epsilon)	2	Z'Lyte
INSR	10	Z'Lyte
INSRR (IRR)	-1	Z'Lyte
IRAK4	-6	Z'Lyte
ITK	2	Z'Lyte
JAK1	0	Z'Lyte
JAK2 JH1 JH2 V617F	0	Z'Lyte
JAK2 JH1 JH2	-3	Z'Lyte
JAK2	4	Z'Lyte
JAK3	1	Z'Lyte
KDR (VEGFR2)	7	Z'Lyte
KIT T670I	1	Z'Lyte
KIT V559D V654A	-1	Z'Lyte
KIT V559D	-1	Z'Lyte
KIT V560G	-5	Z'Lyte
KIT	-2	Z'Lyte
KSR2	2	Z'Lyte
LCK	12	Z'Lyte
LTK (TYK1)	-1	Z'Lyte
LYN A	-2	Z'Lyte
LYN B	-2	Z'Lyte
MAP2K1 (MEK1)	-2	Z'Lyte
MAP2K2 (MEK2)	2	Z'Lyte
MAP2K6 (MKK6)	3	Z'Lyte
MAP3K19 (YSK4)	3	Z'Lyte
MAP3K8 (COT)	-6	Z'Lyte

MAP3K9 (MLK1)	17	Z'Lyte
MAP4K2 (GCK)	5	Z'Lyte
MAP4K4 (HGK)	1	Z'Lyte
MAP4K5 (KHS1)	5	Z'Lyte
MAPK1 (ERK2)	-1	Z'Lyte
MAPK10 (JNK3)	0	Z'Lyte
MAPK11 (p38 beta)	-8	Z'Lyte
MAPK12 (p38 gamma)	7	Z'Lyte
MAPK13 (p38 delta)	5	Z'Lyte
MAPK14 (p38 alpha) Direct	3	Z'Lyte
MAPK14 (p38 alpha)	1	Z'Lyte
MAPK3 (ERK1)	6	Z'Lyte
MAPK7 (ERK5)	5	Z'Lyte
MAPK8 (JNK1)	3	Z'Lyte
MAPK9 (JNK2)	-15	Z'Lyte
MAPKAPK2	10	Z'Lyte
MAPKAPK3	17	Z'Lyte
MAPKAPK5 (PRAK)	3	Z'Lyte
MARK1 (MARK)	-10	Z'Lyte
MARK2	6	Z'Lyte
MARK3	2	Z'Lyte
MARK4	-4	Z'Lyte
MATK (HYL)	-2	Z'Lyte
MELK	31	Z'Lyte
MERTK (cMER)	2	Z'Lyte
MET (cMet) Y1235D	4	Z'Lyte
MET (cMet)	-1	Z'Lyte
MET M1250T	0	Z'Lyte
MINK1	7	Z'Lyte
MKNK1 (MNK1)	4	Z'Lyte
MST1R (RON)	2	Z'Lyte
MST4	1	Z'Lyte
MUSK	-10	Z'Lyte
MYLK2 (skMLCK)	7	Z'Lyte
NEK1	-1	Z'Lyte
NEK2	-4	Z'Lyte
NEK4	4	Z'Lyte
NEK6	-3	Z'Lyte
NEK9	0	Z'Lyte
NIM1K	-2	Z'Lyte

NTRK1 (TRKA)	19	Z'Lyte
NTRK2 (TRKB)	1	Z'Lyte
NTRK3 (TRKC)	2	Z'Lyte
PAK1	6	Z'Lyte
PAK2 (PAK65)	-1	Z'Lyte
PAK3	-7	Z'Lyte
PAK4	3	Z'Lyte
PAK6	-2	Z'Lyte
PAK7 (KIAA1264)	-5	Z'Lyte
PASK	-4	Z'Lyte
PDGFRA (PDGFR alpha)	2	Z'Lyte
PDGFRA D842V	-1	Z'Lyte
PDGFRA T674I	0	Z'Lyte
PDGFRA V561D	2	Z'Lyte
PDGFRB (PDGFR beta)	0	Z'Lyte
PDK1 Direct	7	Z'Lyte
PDK1	0	Z'Lyte
PEAK1	1	Z'Lyte
PHKG1	-1	Z'Lyte
PHKG2	-2	Z'Lyte
PIM1	8	Z'Lyte
PIM2	-4	Z'Lyte
PIM3	12	Z'Lyte
PKN1 (PRK1)	1	Z'Lyte
PLK1	6	Z'Lyte
PLK2	5	Z'Lyte
PLK3	28	Z'Lyte
PRKACA (PKA)	1	Z'Lyte
PRKCA (PKC alpha)	13	Z'Lyte
PRKCB1 (PKC beta I)	2	Z'Lyte
PRKCB2 (PKC beta II)	15	Z'Lyte
PRKCD (PKC delta)	3	Z'Lyte
PRKCE (PKC epsilon)	6	Z'Lyte
PRKCG (PKC gamma)	-4	Z'Lyte
PRKCH (PKC eta)	-9	Z'Lyte
PRKCI (PKC iota)	-10	Z'Lyte
PRKCN (PKD3)	8	Z'Lyte
PRKCQ (PKC theta)	8	Z'Lyte
PRKCZ (PKC zeta)	-1	Z'Lyte
PRKD1 (PKC mu)	-2	Z'Lyte

PRKD2 (PKD2)	-4	Z'Lyte
PRKG1	-6	Z'Lyte
PRKG2 (PKG2)	1	Z'Lyte
PRKX	5	Z'Lyte
PTK2 (FAK)	2	Z'Lyte
PTK2B (FAK2)	-1	Z'Lyte
PTK6 (Brk)	-4	Z'Lyte
RAF1 (cRAF) Y340D Y341D	-9	Z'Lyte
RET A883F	-1	Z'Lyte
RET S891A	-3	Z'Lyte
RET V804E	2	Z'Lyte
RET V804L	1	Z'Lyte
RET Y791F	5	Z'Lyte
RET	5	Z'Lyte
ROCK1	2	Z'Lyte
ROCK2	1	Z'Lyte
ROS1	-6	Z'Lyte
RPS6KA1 (RSK1)	-1	Z'Lyte
RPS6KA2 (RSK3)	0	Z'Lyte
RPS6KA3 (RSK2)	10	Z'Lyte
RPS6KA4 (MSK2)	-4	Z'Lyte
RPS6KA5 (MSK1)	2	Z'Lyte
RPS6KA6 (RSK4)	4	Z'Lyte
RPS6KB1 (p70S6K)	3	Z'Lyte
RPS6KB2 (p70S6Kb)	-4	Z'Lyte
SBK1	6	Z'Lyte
SGK (SGK1)	4	Z'Lyte
SGK2	3	Z'Lyte
SGKL (SGK3)	0	Z'Lyte
SNF1LK2	-5	Z'Lyte
SRC N1	5	Z'Lyte
SRC	14	Z'Lyte
SRMS (Srm)	2	Z'Lyte
SRPK1	1	Z'Lyte
SRPK2	-4	Z'Lyte
STK22B (TSSK2)	-2	Z'Lyte
STK22D (TSSK1)	6	Z'Lyte
STK23 (MSSK1)	-2	Z'Lyte
STK24 (MST3)	4	Z'Lyte
STK25 (YSK1)	-7	Z'Lyte

STK3 (MST2)	-2	Z'Lyte
STK4 (MST1)	-5	Z'Lyte
SYK	1	Z'Lyte
TAOK2 (TAO1)	-1	Z'Lyte
TBK1	4	Z'Lyte
TEK (TIE2) Y897S	2	Z'Lyte
TEK (Tie2)	5	Z'Lyte
TNK1	-3	Z'Lyte
TXK	4	Z'Lyte
TYK2	0	Z'Lyte
TYRO3 (RSE)	-5	Z'Lyte
YES1	-6	Z'Lyte
ZAP70	4	Z'Lyte

Figure S1.

Docking poses from pyronaridine and all tested analogs. PL^{pro} surface is colored according to its electrostatic potential.

